1 # Tectonic interactions during rift linkage: Insights from analog and

2 # numerical experiments

4 *Timothy Chris Schmid[1], Sascha Brune[2,3], Anne Glerum[2], and Guido Schreurs[1]*

6 *[1]Institute of Geological Sciences, University of Bern*

7 *[2]Helmholtz Centre Potsdam – GFZ German Research Centre for Geosciences, Potsdam, Germany*

8 *[3]Institute of Geosciences, University of Potsdam, Potsdam, Germany*

10 *Corresponding author Timothy Schmid: timothy.schmid@geo.unibe.ch*

11 *Institute of Geological Sciences, University of Bern, Baltzerstrasse 1+3, CH-3012 Bern, Switzerland*

13 ***Keywords:*** *Numerical modelling, analog modelling, stress deflection, rift interaction, rift*

14 *propagation*

16 **Abstract**

17 Continental rifts evolve by linkage and interaction of adjacent individual segments. As rift

18 segments propagate, they can cause notable re-orientation of the local stress field so that

19 stress orientations deviate from the regional trend. In return, this stress re-orientation can

20 feed back on progressive deformation and may ultimately deflect propagating rift segments

21 in an unexpected way. Here, we employ numerical and analog experiments of continental

22 rifting to investigate the interaction between stress re-orientation and segment linkage. Both

23 model types employ crustal-scale two-layer setups where pre-existing linear heterogeneities

24 are introduced by mechanical weak seeds. We test various seed configurations to investigate

25 the effect of i) two competing rift segments that propagate unilaterally, ii) linkage of two

26 opposingly propagating rift segments, and iii) the combination of these configurations on

27 stress re-orientation and rift linkage. Both the analog and numerical models show counter-

28   intuitive rift deflection of two sub-parallel propagating rift segments competing for linkage

29   with an opposingly propagating segment. The deflection pattern can be explained by means

30   of stress analysis in numerical experiments where stress re-orientation occurs locally and

31   propagates across the model domain as rift segments propagate. Major stress re-orientations

32   may occur locally, which means that faults and rift segment trends do not necessarily align

33   perpendicularly to far-field extension directions. Our results show that strain localization and

34   stress re-orientation are closely linked, mutually influence each other and may be an important

35   factor for rift deflection among competing rift segments as observed in nature.

1. Introduction

38   Continental rifting involves brittle faulting and the formation of subsiding rift basins. In places

39   where individual rift segments are in proximity, they may interact and link when segments

40   propagate and the rift system matures (Morley et al., 1990; Nelson et al., 1992; Rosendahl,

41   1987). The propagation and linkage of formerly isolated rift segments resembles the

42   propagation and interaction of extension fractures on a micro-scale (e.g., Childs et al., 1995;

43   Willemse, 1997; Willemse et al., 1996; Fig. 1a). Indeed, analytical solutions and models have

44   been used to describe crack growth and to predict its direction (e.g., Macdonald and Fox,

45   1983; Mills, 1981). Such cracks occur in a variety of materials over a vast order of magnitude

46   in length scale from micro-scale cracks in glass to km-scale ridge interaction structures in

47   oceanic crust (Pollard and Aydin, 1984; Fig. 1a).

48

49   Propagation and interaction of individual rift segments occur in continental rift systems at

50   various styles and scales (Fig. 1b) and have been intensively studied over the years. The East

51   African Rift System (EARS) constitutes a narrow rift with an Eastern and Western branch that

52   propagate southward and northward, respectively (EARS; e.g., Ebinger et al., 2000; Morley

53   et al., 1990; Nelson et al., 1992; Bonini et al., 2005; Bosworth, 1985; Brune et al., 2017; Corti

et al., 2019; Glerum et al., 2020; Heilman et al., 2019; Koehn et al., 2008; Kolawole et al., 2018) comprising different sub-parallel deformed regions (inset Fig. 1c). On smaller scale, interaction of segmented grabens has been studied for example in in the Canyonlands National Park, Utah, a part of the Basin and Range wide rift (Allken et al., 2013; Trudgill, 2002; Schultz-Ela and Walsh, 2002), where various styles of graben interaction are attributed to the underlying strata (e.g., salt layer) or pre-existing weaknesses (Fig. 1d).
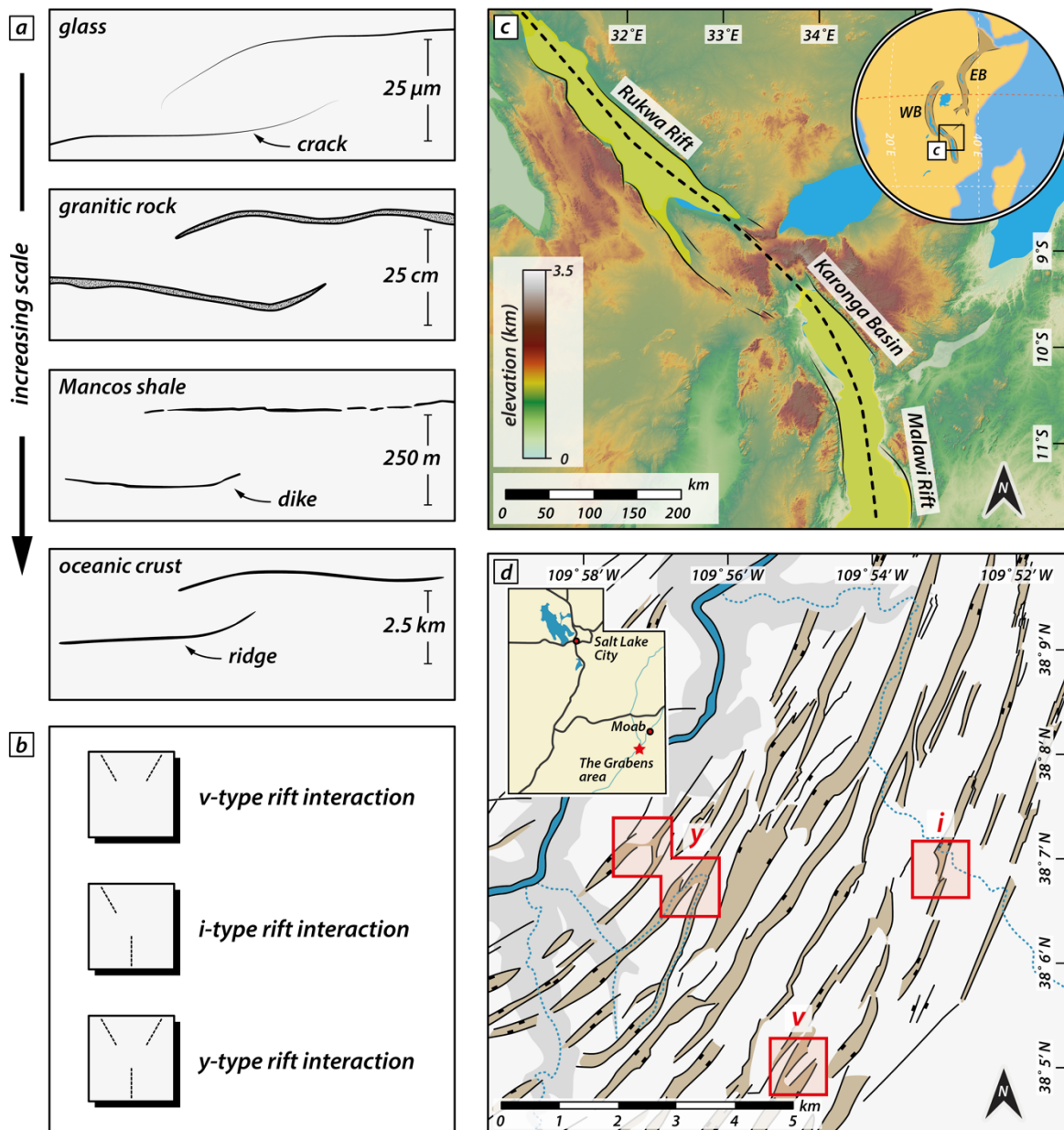
Figure 1: Similar linkage structures occurring at a vast range of spatial scales. a) Propagation and linkage of segments at different scale from micro cracks in glass to linkage of oceanic ridge segments. Redrawn after Pollard and Aydin, (1984). b) Rift-interaction types investigated in this study. c) Rukwa Rift and Malawi rift along the Western Branch of the East African Rift System (EARS; inset). The two basins link obliquely via the Karonga Basin and form an i-type interaction zone. Rift axis redrawn after Kolawole et al., (2021). WB: Western Branch; EB: Eastern Branch of the EARS. d) Rift-related linked graben structures in the Canyonlands National Park, USA. Red rectangles mark areas with distinct interaction geometries (v-, i-, and y-geometries; see b) and text for detail). Redrawn after Allken et al., (2013).

Structural inheritance is thought to control nucleation and strain distribution along newly formed normal faults, as weak fabrics can precondition and weaken a heterogenous upper crust (e.g., Collanega et al., 2018; Heilman et al., 2019; Kolawole et al., 2018; Morley, 2010; Morley, 1999; Kolawole et al., 2021; Morley et al., 2004). Pre-existing weak fabrics may appear as large shear zones (Daly et al., 1989), suture zones along adjacent basement terranes (Corti, 2012; Corti et al., 2007) or upper crustal fabrics. Resulting rift structures may form as initially isolated segments that propagate along strike, interact and evolve into continuous zones of deformation as they link (Nelson et al., 1992). Rift segments link through previously un-rifted interaction zones resulting in a characteristic geometry that persists during later rift stages (Nelson et al., 1992).

Recent strain accommodation in the Rukwa-North Malawi segment of the western branch of the EARS (Fig. 1c) shows dominant dip-slip faulting parallel to the border faults (Kolawole et al., 2018; Morley, 2010) driven by the reactivation of pre-existing basement fabrics (Heilman et al., 2019). There, the concentration of seismicity in the SE and NW of the Rukwa and Northern Malawi Rift, respectively suggest subsequent propagation and linkage of the rift segments with a flip in the boundary fault polarity near the interaction zone (Heilman et al., 2019 and references therein).

90   Pre-existing structures as well as fault interaction across multiple scales disturb the regional

91   stress orientation (Morley, 2010; Oliva et al., 2022). In return, stress re-orientations within

92   and adjacent to rift segments influence the style of progressive deformation. Ultimately, stress

93   re-orientation may even favor pure dip-slip behavior even for extensional faults with an

94   oblique orientation to the regional extension (e.g., Morley, 2010; Corti et al., 2013; Morley,

95   2017; Philippon et al., 2015). This interplay between pre-existing structures and local re-

96   orientation of the regional stress field affects how propagating rift segments interact. Under

97   favorable conditions, it may even cause deflection of propagating rift segments (Nelson et al.,

98   1992).

99

100 Rift propagation and segment interaction has been investigated by analog modelling studies

101 that examined linkage of two segments across a transfer zone (e.g., Zwaan et al., 2016;

102 Zwaan and Schreurs, 2017; Corti, 2012; Acocella et al., 1999; Bellahsen and Daniel, 2005).

103 Bellahsen and Daniel (2005) studied the control of existing faults on new fault growth under

104 multiphase extension. They suggested that pre-existing faults may disturb the local stress field

105 and impede linkage of newly forming faults which also occurs in natural examples of

106 multiphase extension (Duffy et al., 2015). Such stress deflections due to the vicinity of pre-

107 existing faults have been reported and studied in natural settings such as the North Malay

108 Basin, Thailand, (Tingay et al., 2006; Tingay et al., 2010). While analog experiments are an

109 effective tool to simulate mechanical (brittle and ductile) deformation processes, accessing

110 information about stresses is challenging. In contrast, numerical modelling experiments

111 provide direct access to element-wise stress tensors that can be interpreted in terms of stress

112 regimes and orientations under extension (Brune and Autin, 2013; Duclaux et al., 2020).

113 Despite the impact of stress distribution on faulting and rift segment interaction, only recently

114 numerical studies made use of it to gain further insights into rift evolution and continental

115 break-up (e.g., Glerum et al., 2020; Mondy et al., 2018). However, these studies mostly focus

116   on larger-scale deformation to evaluate stresses over the entire time span of rifting up to

117   continental break-up.

118

119   Here we use crustal-scale analog and numerical models to investigate rift propagation and

120   strain localization in early rifting stages when rift segments interact. Both types of models

121   document enigmatic rift segment deflection when two sub-parallel rift segments propagate

122   approximately in the same direction and compete for linkage with an opposingly propagating

123   segment. To understand the reason for rift segment deflection, we analyze the stress

124   distribution in early rifting stages and its interplay with strain localization that initiates above

125   pre-existing structures. Our experiments show that relatively simple rift segment interactions

126   can cause locally complex stress patterns that deviate from the regional stress field. Such

127   stress re-orientations occur in transient stages and can change over time and with progressive

128   deformation due to changes in material strengths.

129

2. Analog model

The presented analog modelling experiment shows unexpected features such as rift deflection. It motivates our numerical study, and we use the analog model as a reference for examining strain and stress distribution in numerical experiments.

2.1. Analog model setup

For the analog reference model, we use a simplified two-layer crustal scale setup with a brittle and a viscous material to simulate upper crustal brittle faulting and lower crustal viscous deformation, respectively. The base of the model consists of a set of alternating plexiglass and foam bars which are compressed prior to the model preparation by two mobile sidewalls (Fig. 2a). During the experiment the computer-controlled sidewalls extend and provide a symmetric velocity gradient as the model base expands and the model vertically thins. For monitoring the surface deformation evolution, we use a stereoscopic camera setup to take top view photos and stereo image pairs every 60 s for quantitative deformation analysis by means of 3D stereo Digital Image Correlation (Adam et al., 2005). The model was scanned every 20 min in a medical XRCT scanner for gaining insights on internal model evolution.
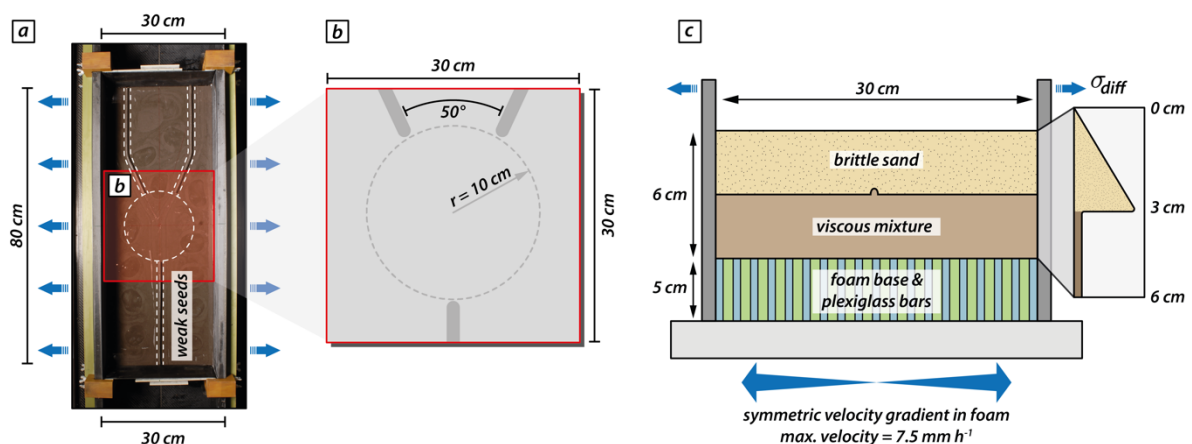
Figure 2: Analog modelling setup. a) Top view of the experimental apparatus with two mobile side walls that extend orthogonally. The entire model comprises an area of 80 x 30 cm and three viscous seeds are placed on top of the viscous layer before sieving in the brittle sand layer. The central model part where propagating rift segments interact contains no seeds.

156

2.2.   Model geometry, rheological layering, and material properties

158   For simulating upper crustal deformation, we use dry quartz sand with a bulk density of 1560

159   kg m^{-3} and an internal friction coefficient of 0.72 (Schmid et al., 2020a). For the lower viscous

160   model part, we use a quasi-Newtonian PDMS/corundum sand mixture (weight ratio 1:1) with

161   bulk density of 1600 kg m^{-3} and a viscosity of $\sim 1 \times 10^5$ Pa s (Zwaan et al., 2018). Hence, the

162   brittle-viscous setup has a density gradient that avoids density instabilities and spontaneous

163   upwelling of the viscous layer. The model features viscous rods placed on top of the viscous

164   model layer before sieving in the quartz sand (Fig. 2). These rods act as mechanically weak

165   seeds and localize faulting in the upper brittle model domain. The used seed configuration

166   includes three individual seed segments. The model includes a y-seed configuration with one

167   seed segment perpendicular to the extension direction on one side (hereafter called frontal

168   segment) whereas on the opposing side of the model center two obliquely placed seeds

169   (hereafter called rear segments) form an intermediate angle of 50° (Fig. 2; see also Fig. 1b,d).

170   The three seed segments hypothetically merge at the model center. However, we exclude

171   weak seeds in an area with a radius r = 10 cm around the model center to allow free

172   interaction of the propagating rift structures (Fig. 2b). The analog model comprises an initial

173   area of 80 cm by 30 cm and has a total thickness of 6 cm (each layer 3 cm) which represents

174   a 30 km thick continental crust. In accordance with the numerical setup, the effectively

175   analyzed model area is restricted to 30 x 30 cm. The mobile sidewalls move with an extension

176   velocity of 5 mm h^{-1} each (totaling in 10 mm h^{-1}), which results in a maximum extension of

177   40 mm at the final model stage after 4h.

178

2.3. Analog model results

In the analog model three different rift segments initiate above the weak seeds and propagate toward each other. Thereby, the two rear segments compete for linkage with the frontal segment. After 30 min (i.e., 5 mm extension; Fig. 3(i)), brittle deformation localizes along two rift boundary faults forming the frontal rift segment. Rifting in the rear segments localizes first along right-dipping rift boundary faults and after 60 min (i.e., 10 mm extension; Fig. 3(ii)) both rear segments develop a set of two conjugate rift boundary faults (Fig. 3a,b (ii)). Interestingly, instead of advancing straight forward, the fault tips deflect and propagate away from each other (Fig. 3b,d (ii)). This is partially due to the rift propagation over the area where no seeds are present where rifting perpendicular to the extension direction is favored. However, after 120 min (i.e., 20 mm extension; Fig. 3 (iii)) rift tips deflect and turn away from one another. Rift tips deflect from an initially oblique orientation and rotate into an inverted oblique direction (with respect to the extension direction). The frontal and the rear left rift segment propagate further and, as they approach one another, form an en-echelon basin that convergently overlaps with the frontal rift segment (Morley et al., 1990; Fig. 3b,d (iii)). After 180 min (i.e., 30 mm extension; Fig. 3(iv)), intra-rift faults develop in the frontal and left rear rift segments. Note that strain rate is successively localized in the two fully linked rift segments whereas the right rear segment experiences minor strain rate values (Fig. 3d (iv)). At the final model stage (i.e., after 240 min and 40 mm extension; Fig. 3 (v)), the right rear segment propagated minimally with a rift tip turned away from the linked segments (Fig. 3b,d (v)). The fully linked frontal and left rear segments continuously accommodated displacement resulting in deeper rift structures compared to the abandoned right rear segment (Fig. 3c,e (v)).
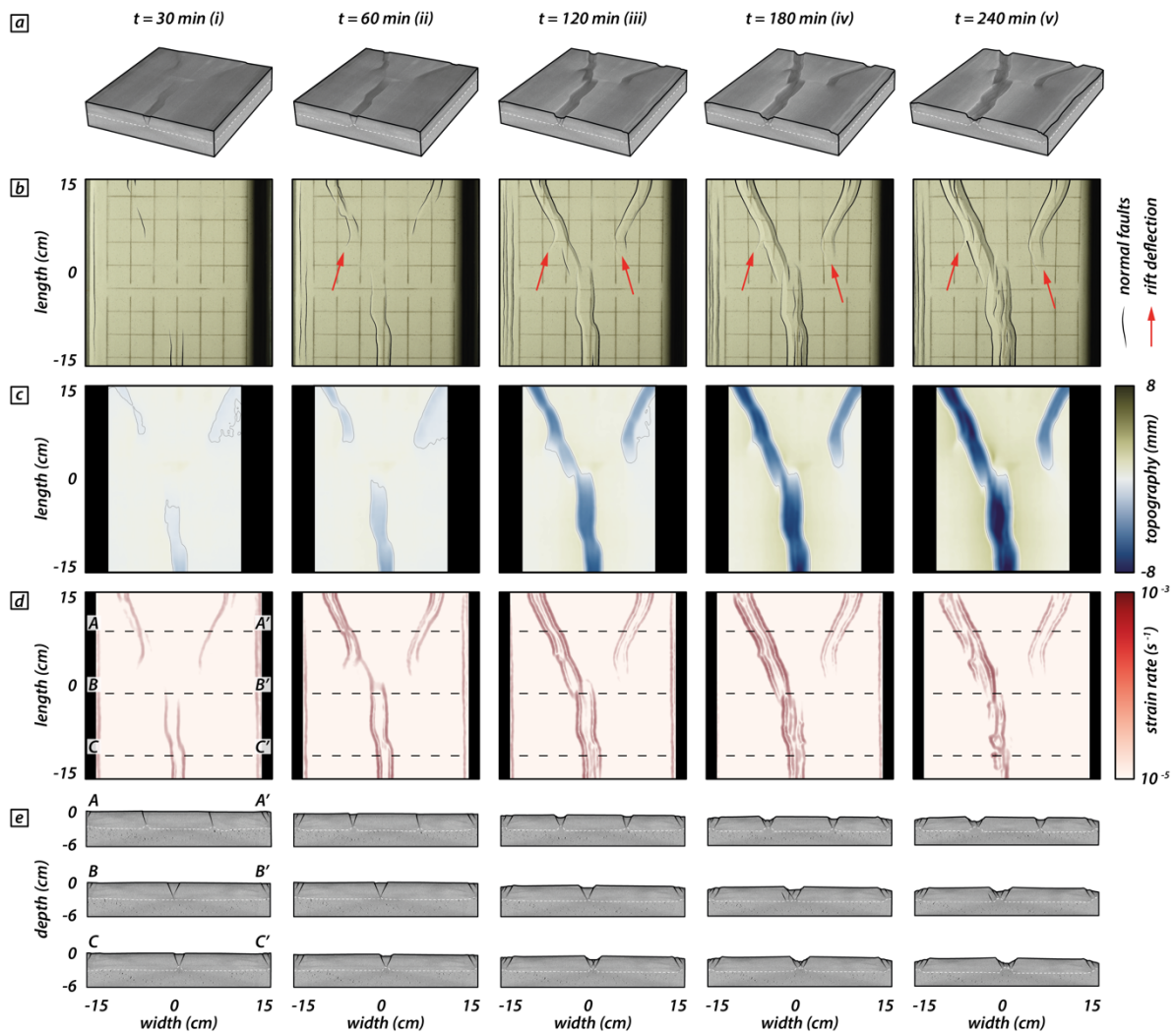
Figure 3: *Analog modelling results documenting deflection of the right rear segment and cessation of faulting activity. Distinct time steps (i.e., after 30 min and after every hour) show the model evolution. a) CT volumes of the investigated model domain at distinct time steps. White dashed lines indicate the brittle-viscous interface. b) Top views and line drawings indicating observable normal faults at the model surface. Red arrows indicate rift tips that deflect and turn away from one another. c) Topography from digital elevation models of the model surface. d) Strain rates obtained from 3D stereo DIC. Black dashed lines indicate positions of 3 transects through the CT volume. e) Rift transects A-A', B-B', and C-C'. White dashed lines indicate the brittle-viscous interface.*

3. Numerical modelling

We perform a series of numerical models to investigate rift linkage interaction and to analyze occurring surface stresses. Similar to the analog experiment, the numerical model consists of a two-layer crustal setup with laterally homogenous material layers where boundary-orthogonal extension with constant velocity is applied.

3.1. Numerical model setup

We use the open source, finite-element code ASPECT to solve the extended Boussinesq equations of momentum, mass, and energy in combination with advection equations for each compositional field (Gassmöller et al., 2018; Glerum et al., 2018; Heister et al., 2017; Kronbichler et al., 2012; Rose et al., 2017; Glerum et al., 2020). Since the numerical models are motivated by the analog model, the two setups are designed in a similar way. To this aim, we employ a numerical setup where the rheologies of upper and lower crust are brittle and ductile, respectively, and independent of temperature just like in the analog model. However, the numerical models operate on the true scales of the continental crust over tens of kilometers and millions of years, while the analog model is a scaled, cm-sized representation that evolves on hour-scale. Additionally, the numerical setup applies maximum extension velocities at the side walls and extension velocities at the base that linearly increase from the center towards the model boundaries. In contrast, maximum extension velocities at the side walls in the analog model are achieved via compression of a basal foam plexiglass setup (prior to the model run) that extends homogeneously during the model run.

The presented numerical experiments cover a rectangular cuboid domain of 150 km width and length in the horizontal x- and y-direction, respectively, and 30 km in depth along the vertical z-axis (Fig. 4a). The entire model domain is divided into 1.53 million hexahedral, second-order elements. For the upper 15 km of the model, we use a cell resolution of 750 m, with an additional refinement at the uppermost km which yields near-surface elements with a resolution of 375 m. The grid resolution for the lower 15 km of the model is 1500 m. At the left and right model sides, we apply a symmetrically distributed outflow velocity of ½ V_x = 5 mm yr^{-1}, resulting in a total extension velocity of 10 mm yr^{-1} (Fig. 4a,b). After a total model time of 4 My, the model has therefore experienced a total extension of 40 km. While V_x is prescribed at the left and right model sides, V_y and V_z are left free. We compensate material

243   loss through the side boundaries by compensational inflow at the model base (Fig. 4b). The

244   front and back lateral boundaries allow for free slip and the top of the model features a free

245   surface boundary condition (Rose et al., 2017).

246

247   The model includes two rheological layers represented by compositional fields, namely a 15

248   km thick visco-plastic upper crust with a density of 2700 kg m^{-3} and a 15 km thick iso-viscous

249   lower crust with a density of 2900 kg m^{-3} and a constant viscosity of $1 \cdot 10^{20}$ Pa s. For the upper

250   crust, the viscous viscosity is fixed to $2 \cdot 10^{28}$ Pa s, such that plastic deformation is always

251   enabled. We introduce initial and dynamic mechanical weaknesses in the upper crust in two

252   ways. (i) Mechanically weak seeds: At distinct positions near the brittle-ductile interface, the

253   upper model layer is locally 10% thinned and the lower model layer elevates like the viscous

254   weak seeds in the analog model setup. These mechanical seeds weaken the upper crustal

255   strength and localize brittle faulting. Our experiments include three different seed

256   configurations: v, i, and y (Fig. 4c; see also Fig. 1b-d), where seeds within a central model

257   area (i.e., r = 100 km) are absent. For each configuration, the rear seeds form an intermediate

258   angle of 10°, 30°, or 50°. (ii) Friction softening: For each element, an initial plastic strain value

259   of 0 (resulting in strong material) to 0.1 (weaker) is randomly assigned and reduces the

260   maximum friction angle of 26.56° by a maximum of 10%. This reflects the structural

261   heterogeneity of natural settings and allows for more randomized strain patterns in the central

262   model domain where the mechanical seeds are absent. The initial plastic strain noise is

263   distributed over the entire model width with an amplitude following a Gaussian curve parallel

264   to the extension direction that is repeated along the model length (y-direction, Fig. 4d). During

265   continuous extension, the effective friction angle linearly reduces to 25% of the maximum

266   friction angle (i.e., to 6.64°) for plastic strain between 0 and 1 while it remains constant at

267   6.64° for plastic strains > 1 (Fig. 4e). This corresponds to a reduction of the effective friction

268   coefficient from 0.5 to 0.12. The cohesion of the upper crust remains constant at 5·10⁶ Pa for

269   all conducted experiments.

270
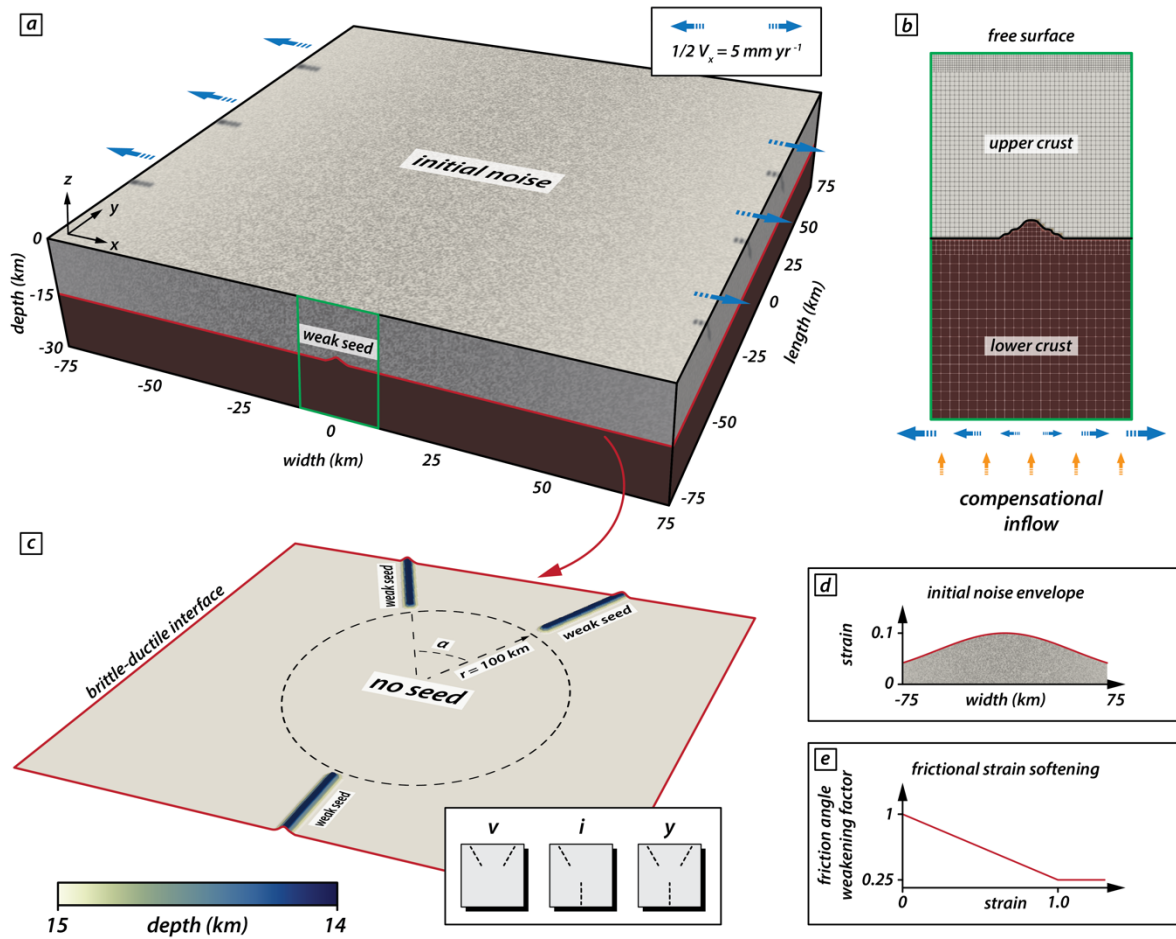
271
272
273   **Figure 4:** *Numerical model setup for iso-viscous models. a) The model domain comprises a volume of 150 x 150 x 30 km. Blue*
274   *arrows indicate the applied boundary-orthogonal extension. The green rectangle indicates the position of the zoom-in in b).*
275   *The red line indicates the initial depth of the brittle-ductile interface (as defined by the interface between the two rheological*
276   *layers) indicated in c). b) Initial conditions and mesh refinement (arrows not to scale). c) Position and configuration of the*
277   *mechanical weak seeds at the brittle-ductile interface. The setup comprises an area with radius r = 100 km where no weak*
278   *seeds are present. Three different seed configurations refer to y-, i-, and v-models (see text for details). d) Initial amplitude of*
279   *strain along the x-axis. The Gaussian distribution is constant along the y-axis; also see grey shade in a). Note that while the*
280   *strain amplitude follows a Gaussian distribution, the location of the initial strain is random. e) Linear weakening with strain*
281   *applied to the friction angle.*

282

3.2. Model limitations

Just like the analog model (Sec. 2), our crustal scale two-layer numerical setup does not comprise a lithospheric mantle layer and no asthenosphere. Further, the iso-viscous setup does not account for a temperature-dependent viscosity. However, we focus on an early rifting phase where the influence of the deforming mantle lithosphere can be neglected. The crustal-scale setup strongly limits the computational effort for calculating deformation in 3D (Allken et al., 2011, 2012; Katzman et al., 1995; Zwaan et al., 2016) and hence, our simplifications allow for a higher model resolution; a necessity to depict early stages of rifting and the coalescence of brittle deformation. Several alternative model runs have been performed including a temperature- and pressure-dependent viscosity. Those tests reproduced first-order features (i.e., strain rates, rift geometry and stress distribution) of the presented models in this study, which further justified the choice of a simplified iso-viscous setup. Note that we apply frictional softening as a function of strain within each cell. For simplicity, we do not include normalization accounting for cell size (Lavier et al., 2000) nor viscoplastic regularization techniques (Duretz et al., 2019; Jacquey and Cacace, 2020). Moreover, our model does not include the influence of melting or magma intrusions nor sedimentation and erosion.

3.3. Post-processing

Numerical models pose the advantage that they grant direct access to stress tensors of each individual cell. We exploit this opportunity by investigating surface stresses to deduct the stress regime and the effect of different seed configurations on stress distribution. ASPECT provides post processors that calculate the magnitude and orientation of the maximum horizontal stresses and the Regime Stress Ratio (RSR) (Glerum et al., 2020). This stress regime characterization is calculated according to the scheme of the World Stress Map (Zoback, 1992). The RSR value maps possible stress regimes to an interval between 0 and 3.

309   For isotropic and homogenous materials, the standard rules of Andersonian faulting are

310   applied (Anderson, 1905). For RSR values < 1, faulting occurs in an extensional stress regime

311   whereas for RSR values > 2 compressive stress regimes generate thrust faults. Strike-slip

312   faults occur for values $1 \geq RSR \leq 2$. We extract data of maximum horizontal compressive

313   stress together with the stress regime and investigate them in areas where the strain rate

314   exceeds a threshold of 10^{-16} s^{-1} and deformation occurs. For visualization, surface stresses

315   from an originally unstructured grid are resampled on an equidistant grid.

316

317   **3.4.   General model evolution of the reference model**

318   In this section we describe the numerical modelling results focusing particularly on the general

319   evolution of our reference model with a y-seed configuration and an intermediate seed angle

320   of 50° (Figure 5). At the early stage (i.e., after 0.5 million years), three distinct rift segments

321   develop above the initial seed positions bounded by a pair of conjugate rift boundary faults

322   (Fig. 5a (i)). This early stage is characterized by a symmetric evolution of the two competing

323   rear segments, which results in a symmetric subsidence inside of the graben structures (Fig.

324   5b (i)). For each rift segment, faulting activity is localized along the rift boundary faults. In

325   the central model domain, however, strain rates depict a more distributed deformation pattern

326   with multiple minor faults (Fig. 5c (i)). Note that the two rear segments propagate and show

327   curved fault segments that initially deflect and turn away from each other resulting in rift

328   segments with a curved geometry expressed in the topography (Fig. 5b (i)), similar to the rift

329   evolution in the analog model. Once they overlap with the propagating frontal segment, faults

330   symmetrically curve inwards and towards the frontal segment. The change from localized

331   strain rates above the seeds to distributed strain rate patterns in the central model domain is

332   best seen in transects (Fig. 5d (i)).

333

334   After the first million years, deformation has prominently localized along the left of the two

335   rear segments and along the frontal segment (Fig. 5a,c, (ii)). While deformation in the frontal

336   segment is localized along the rift boundary faults, inward migration occurred in the left rear

337   segment with developing intra-rift faults and only the left-dipping rift boundary fault active.

338   Similarly, the right rear segment shows faulting along the right-dipping rift boundary fault but

339   activity along intra-rift faults is lacking. In the central model domain, formerly distributed

340   deformation localized between the frontal and left rear rift segment (Fig. 5d (ii)). While strain

341   rates indicate a shift from a symmetric to an asymmetric deformation phase, topography is

342   still symmetric which implies that the shift is imminent and has not affected the topography

343   after the first million years (Fig. 5b (ii)).

344

345   After two million years, deformation is entirely localized along the frontal and left rear

346   segment. Only the right-dipping rift boundary fault of the frontal segment is active and inward

347   migration led to a set of pervasive intra-rift faults (Fig. 5a,c (iii)). The left rear segment depicts

348   a similar deformation pattern as in the previous step, but strain mainly accumulates along the

349   left-dipping rift boundary fault causing an asymmetric graben geometry (Fig. 5d (iii)). Note

350   that, after two million years, fault activity along the right rear segment completely ceased with

351   no further strain accumulation visible (Fig. 5a,c,d (iii)). The topography reflects this completed

352   switch from a symmetric to an asymmetric deformation stage with enhanced subsidence along

353   the frontal and left rear segments and their linkage throughout the central model domain (Fig.

354   5b (iii)).

355

356   With ongoing extension, deformation subsequently localizes along the axial rift zone that links

357   the frontal and left rear segments (Fig. 5a,c,d (iv,v)) and faulting activity along rift boundary

358   faults ceases. The linked structure reaches maximum depth inside of the rift after three million

359   years. After four million years, however, the basin experiences minor uplift due to increase

upward motion of the underlying viscous material (Fig. 5d (iv,v)). Note that the basin depth

of the right rear rift segment remains stable after two million years and does not experience

further subsidence nor uplift.
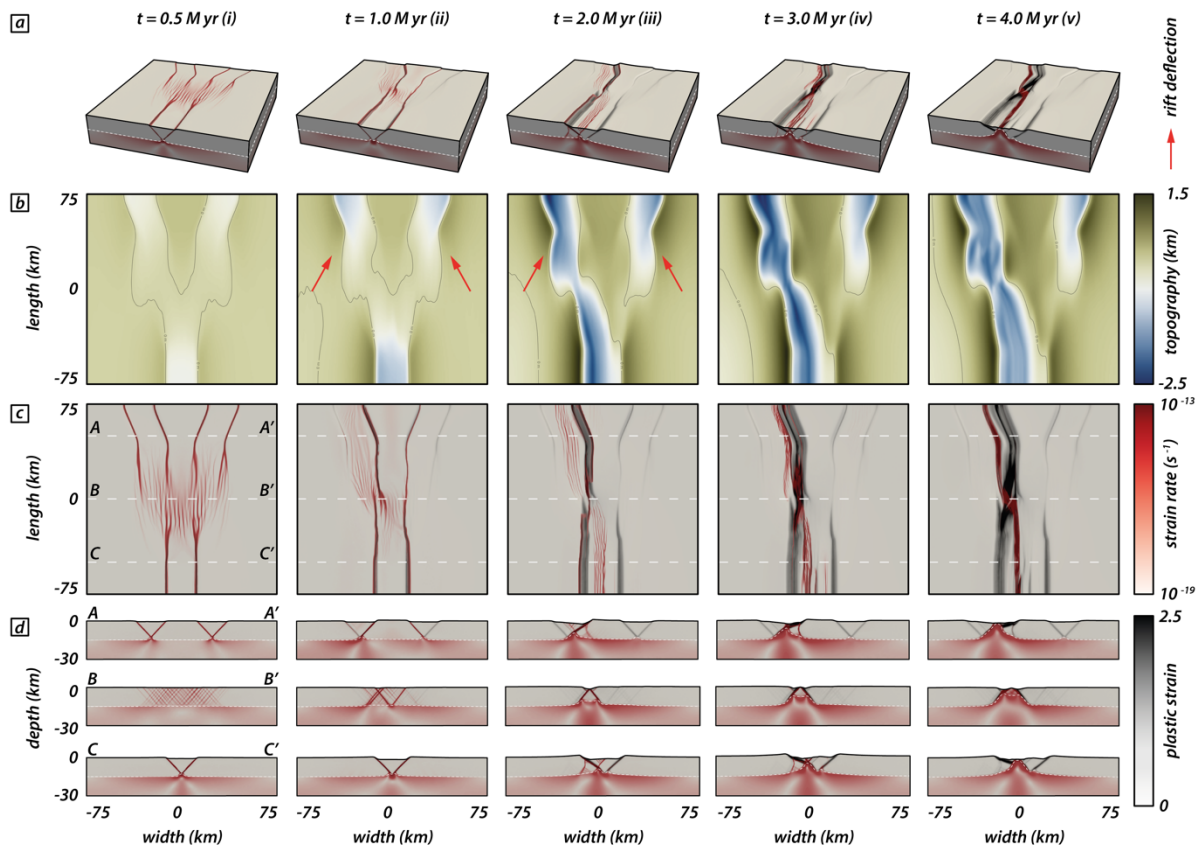
Figure 5: *Modelling results of the reference model documenting cessation of fault activity along the right rear segment while the left rear and frontal segments link. Distinct time steps show the model evolution. a) Model box showing logarithmic strain rates (red) and plastic strain (black) in the brittle and viscous model domain. White dashed lines indicate the brittle-viscous interface. b) Top views showing the model topography. Red arrows indicate rift tips that deflect and turn away from one another. Black lines refer to the zero-elevation height. c) Top views of the model showing strain rates (red) and corresponding plastic strain (black) at distinct model run times. White dashed lines correspond to the three rift transects A-A', B-B', and C-C' in subfigure d). d) Rift-axis perpendicular transects A-A', B-B', and C-C' parallel to the extension direction.*

3.5. Early localization patterns for v-, i-, and y-seeds

To investigate the influence of different seed configurations, we compare v- (Fig. 6a-c), i-

(Fig. 6d-f), and y-seed (Fig. 6g-i) configurations for different intermediate angles (i.e., 10°,

30°, and 50°) at an early stage after 0.5 million years. y- and i-seed configurations provide a

378   setup where rift structures opposingly propagate towards the model center where rift linkage

379   eventually occurs. In contrast, rift structures in the v-seed configuration propagate

380   approximately in the same direction, which has a consequence on the overall strain rate

381   distribution.

382

383   The early stage in v-seed experiments (Fig. 6a-c) is characterized by a zone of localized and

384   distributed deformation in the rear and frontal part of the experiments, respectively. The

385   transition from localized to distributed deformation occurs where the two competing rift

386   segments deflect and rotate away from one another. Note that the fault deflection successively

387   decreases towards the left and right model sides, where faults strike perpendicular to the

388   extension direction. This is consistent with observations for experiments with a y-seed

389   configuration. However, there the two competing rear segments rotate back and eventually

390   bend towards the propagating frontal segment (Fig. 6g-i).

391

392   For experiment with a i-seed configuration (Fig. 6d-f) two opposingly propagating rift branches

393   form. Since the right rear segment is absent, both opposingly propagating rift segments link

394   in the model center where deformation is distributed onto intra-rift faults. The overall strain

395   rate field is localized, and no strain rate deflection occurs.

396

397   Models with a y-seed configuration (Fig. 6g-i) depict a strain rate pattern where deformation

398   is localized along rift boundary faults at the model margins where seeds are present and a

399   distributed en-echelon strain rate pattern in the model center. Note that for the model with

400   an intermediate angle of $10°$ the two competing rear segments are close enough resulting in

401   a zone where strain is localized along only one rift boundary fault per rift segment (i.e.,

402   outward-dipping faults with respect to the model box) that overlap and form a central graben

403   with minor intra-rift faults. For larger intermediate angles, two individual rift segments

404 (bounded by two rift boundary faults) form that propagate towards the model center. While

405 the strain rate pattern due to the competing rear segments is identical for experiments with

406 a y- and v-seed configuration, the additional frontal segment in experiments with a y-seed

407 configuration causes localization of strain rates in a single rift branch bounded by two rift

408 boundary faults. This contrasts with the v-seed configuration where strain rates in the frontal

409 model domain occur distributed over the entire model domain (Fig. 6a-c).

410

411
412
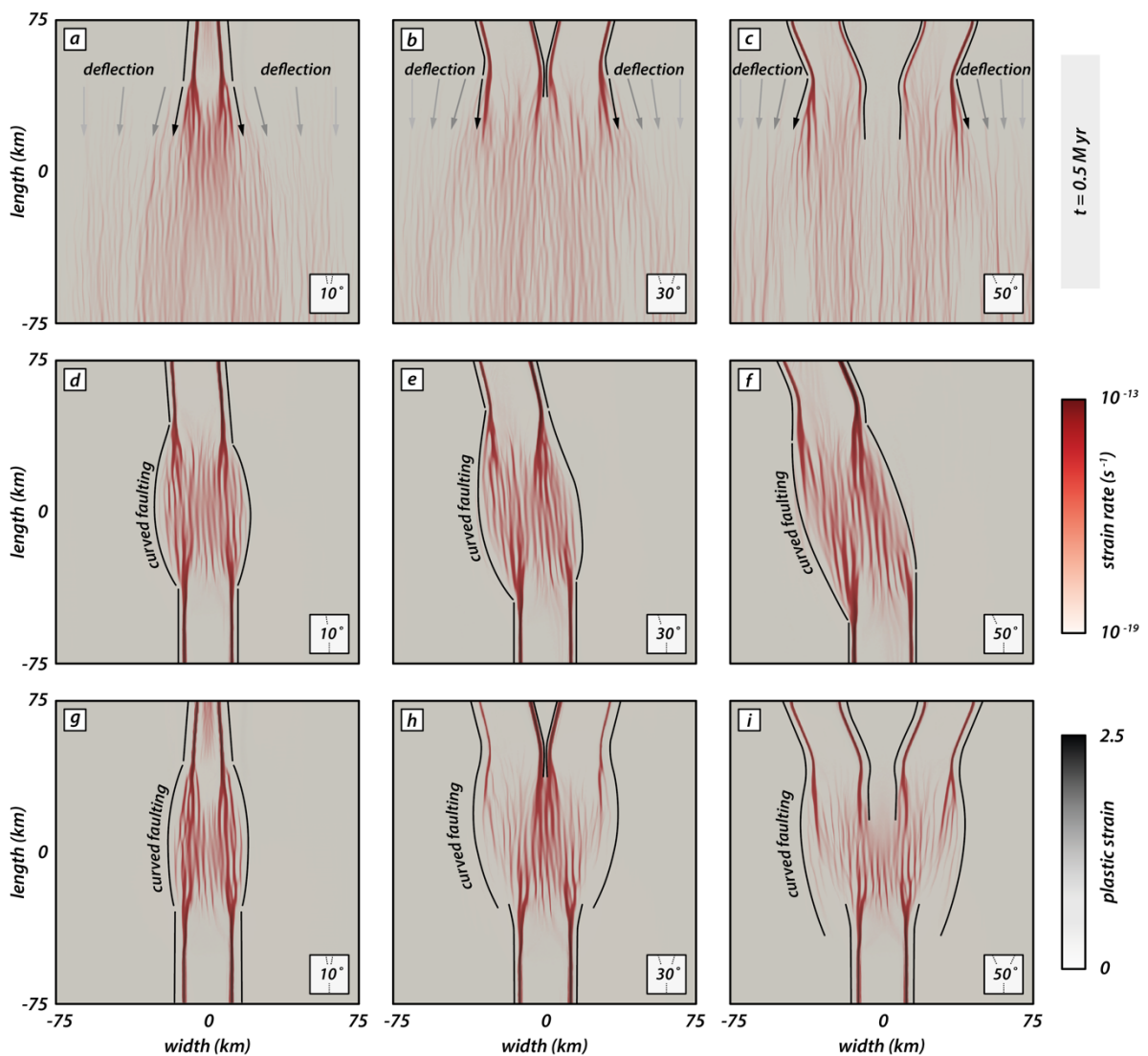
Figure 6: Types of rift segment linkages depending on the seed configuration at an early phase after 0.5 million years. Model top views show strain rates (logarithmic) and plastic strain in red and black colors, respectively. a-c) v-seed configuration for intermediate angles of 10°, 30°, and 50°. d-f) i-seed configuration for intermediate angles of 10°, 30°, and 50°. g-i) y-seed configuration for intermediate angles of 10°, 30°, and 50° (reference model). Black lines confine deformed areas. For models

417   *with a v-seed configuration (a-c), competing rift segments deflect away from each other resulting in a fan-shaped geometry.*
418   *Note that fault strike successively re-orients into an orientation perpendicular to the extension direction towards the left and*
419   *right model sides. Curved faulting occurs in models with an i- and y-seed configuration (d-j) where rift segments interact.*

420

3.6.   Final rift geometry and localization patterns for v-, i-, and y-seeds

422   The final model stage after four million years best illustrates differences in rift geometry

423   between the models with different seed geometry and an intermediate angle (Fig. 7). Rift

424   deflection is well visible in v-seed models (Fig. 7 a-c) and most prominent in experiments with

425   a larger intermediate angle (Fig. 7b,c). Above the seeds, two short individual rift segments

426   form bounded by a pair of conjugate rift boundary faults. However, as the rifts propagate

427   towards the model center, strain is mainly accommodated along the boundary faults that dip

428   towards the model center. Hence, the larger part of the model subsides uniformly and builds

429   a broad rift zone confined by two large boundary faults. When the two rift segments

430   propagate, they deflect and turn away from one another resulting in a gradually wider rift.

431   For intermediate angles of 30° and 50°, both competing rift segments show active faulting

432   along intra-rift faults in the rear model part, but a zone of continuous faulting activity has

433   developed along the right side of the rift.

434

435   Models with an i-seed configuration show a continuous and straight rift geometry for all

436   intermediate angles (fig. 7d-f). For an intermediate angle of 10°, the rift structure is nearly

437   orthogonal with respect to the extension direction. Note that most plastic strain is

438   accommodated along the left-dipping rift boundary fault (Fig. 7d). For larger intermediate

439   angles, the rift subsequently experiences more segmentation with small left stepping

440   segments towards the rear model part (Fig. 7e,f). Strain accommodation occurs mainly on the

441   right-dipping rift boundary fault for the frontal model part and switches to the left-dipping

442   boundary fault in the rear model part.

443
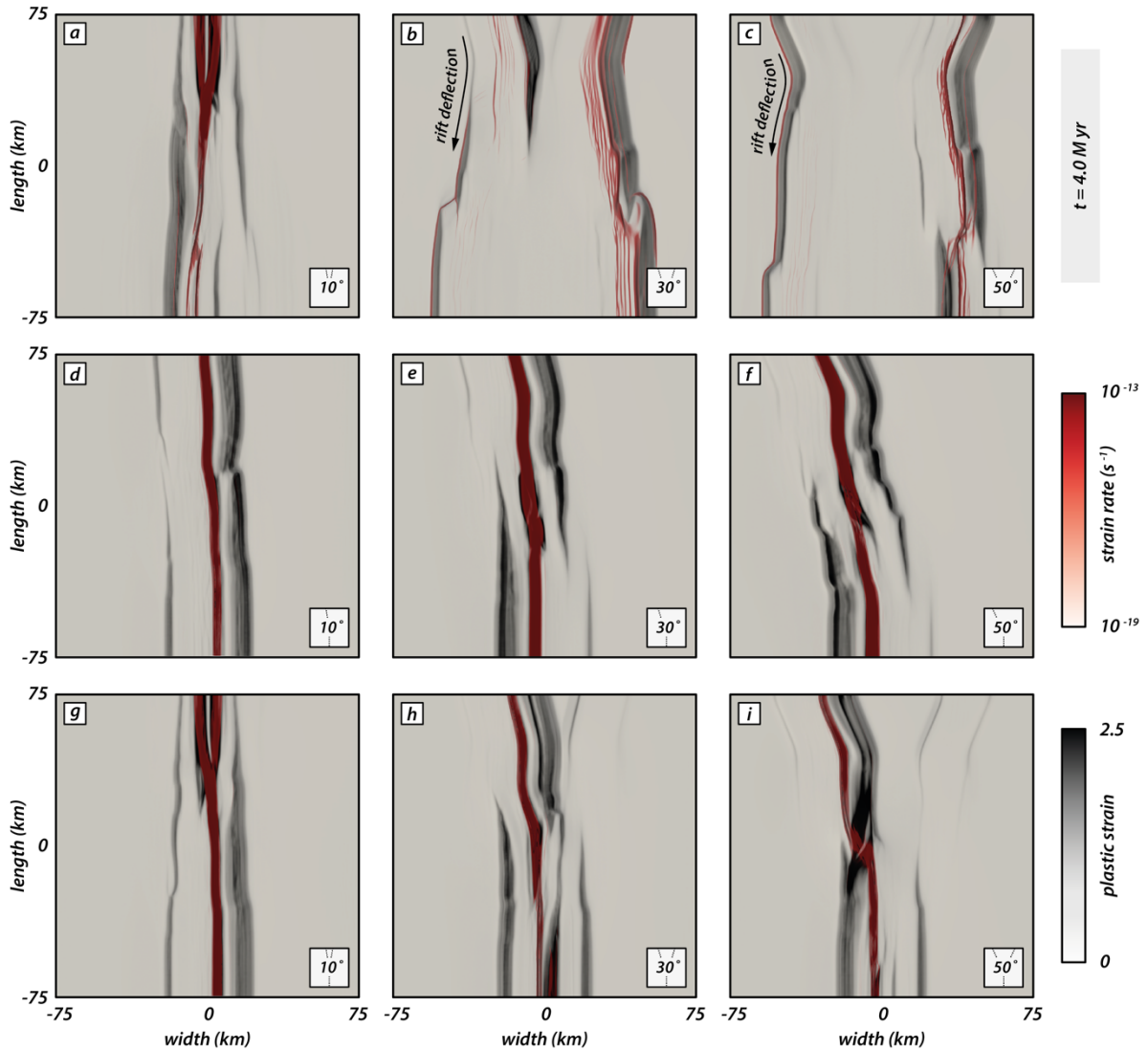
444

445 **Figure 7:** *Influence of seed configuration on the final rift geometry after 4 million years. Strain rates (logarithmic) and plastic*

446 *strain are indicated by red and black colors, respectively. a-c) v-seed configuration for intermediate angles of 10°, 30°, and*

447 *50°. d-f) i-seed configuration for intermediate angles of 10°, 30°, and 50°. g-i) y-seed configuration for intermediate angles*

448 *of 10°, 30°, and 50° (reference model).*

449

450 The most prominent difference occurs in models with a y-seed configuration and various

451 intermediate angles. For an intermediate angle of 10°, the final rift geometry resembles that

452 of a continuous straight rift segment (Fig. 7g). Both competing rear seeds are close enough

453 such that they build one rift system rather than two distinct branches. For y-seed models with

454 a larger intermediate angle (Fig. 7h,i), two individual rear rift segments form and compete for

455 linkage with the frontal rift segment. Plastic strain well illustrates the asymmetric strain

456 accommodation focused along the left-dipping rift boundary fault of the left rear segment,

457 whereas the right rear segment only experienced minor strain accommodation (Fig. 7h,i). In

458 both cases, high strain rates are localized in the axial rift zone and witness activity along the

459 linked frontal and left rear segments.

460

461 Note that all experiments with an intermediate angle of $10°$ (Fig. 7a,d,g) form continuous

462 straight rift segments, regardless of the seed configuration. Additionally, the final rift geometry

463 for y- and v-seed configurations for an intermediate angle of $10°$ is similar with a gently wider

464 rift in the frontal model part (Fig. 7a,g). In contrast, for i-seed configurations the rift width is

465 similar along the entire length with a minor lateral offset (Fig. 7d). Strain rates are localized

466 in the axial rift zone throughout the entire model length forking into two close zones in the

467 rear end where the competing seeds are located.

468

469 **3.7. S_{Hmax} evolution with progressive deformation**

470 In this section we present the distribution and orientation of the maximal horizontal

471 compressive stress component S_{Hmax} with progressive rift evolution and segment linkage. We

472 focus on models with v-, i-, and y-seed configurations and an intermediate angle of $50°$ (Fig.

473 8; see also supplementary Figures S1-S3) distinguishing between model zones with pre-

474 existing structures (i.e., weak seeds) and a central zone where material strength is isotropic.

475

476 Our models depict two distinct phases within the first two million years: early strain

477 accommodation over a wider model domain followed by strain localization and linkage of

478 propagating rift segments (see also supplementary Figures S4-S6). Consequently, we focus

479 on S_{Hmax} in the first two million years of deformation and its effect on rift propagation. Figure

480 8 shows the orientation of S_{Hmax} and the stress regime based on the common color scheme of

481 the World Stress Map (Heidbach et al., 2018). Note that S_{Hmax} orientation and the stress regime

482 alone do not suffice to discriminate between locations where stresses exceed crustal strength

483 and faulting occurs. Strain rate values provide further necessary information, and we use a

484 threshold of 10^{-16} s^{-1} that splits the model into locations of active deformation (i.e., $\geq 10^{-16}$ s^{-1}

485 ^{1}) and tectonically inactive domains (i.e., $< 10^{-16}$ s^{-1}).

486

487

488
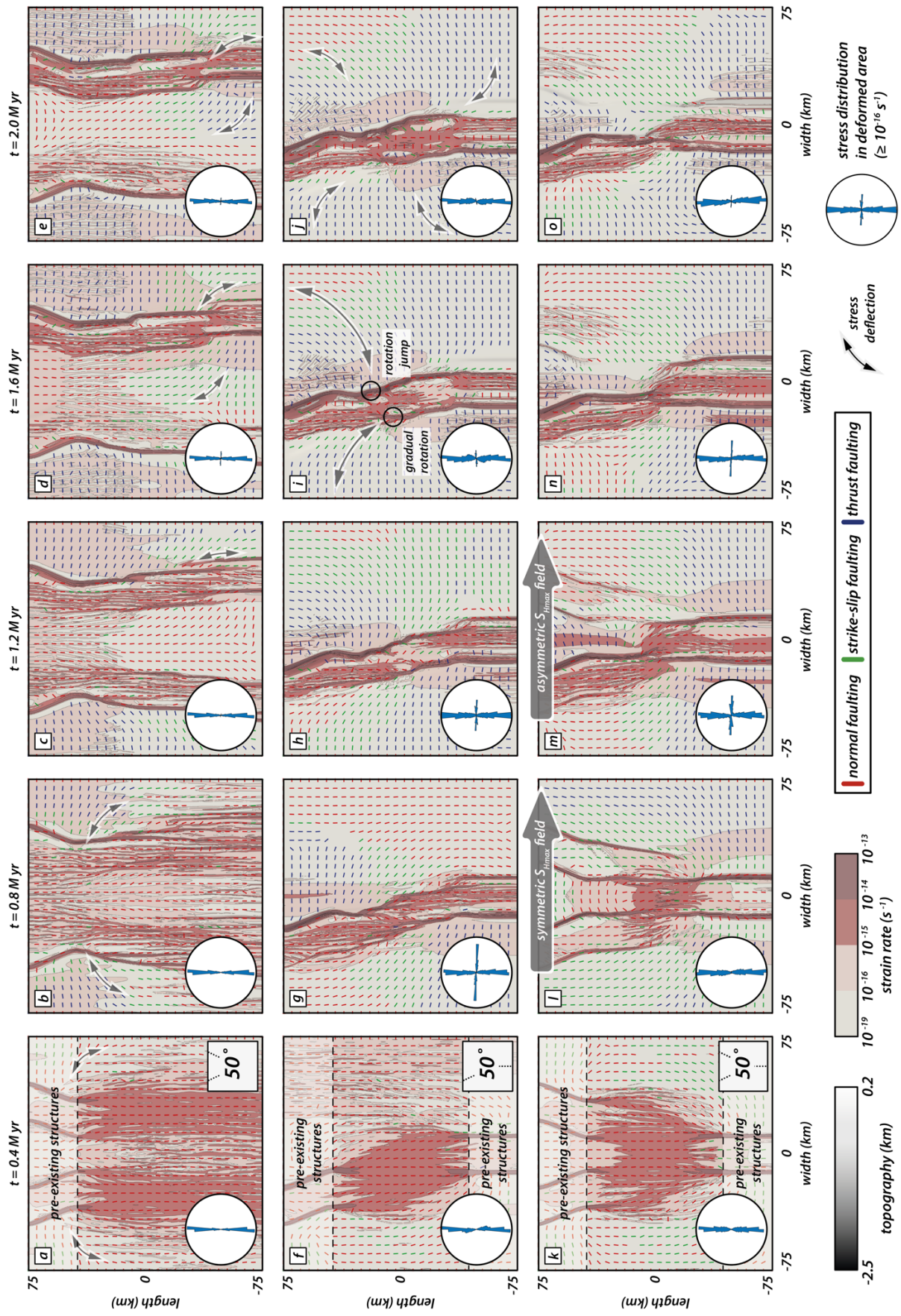
 Figure 8: Interplay of rift localization and surface stresses. Top views show the distribution of the maximum horizontal

compressive stress component S_{Hmax} (not scaled to the magnitude) in models with an intermediate angle of 50° at early

deformation stages (i.e., until 2 million years). a-e) v-seed configuration. f-j) i-seed configuration. k-o) y-seed configuration.

Black colors refer to topographic elevation and red colors mark zones where strain rates exceed a threshold of 10^{-16} s^{-1}. Color

coding for the stress regime marks normal, strike-slip, and thrust faulting in red, green, and blue, respectively, using the

common color scheme of the World Stress Map (Heidbach et al., 2018). Black arrows highlight stress deflection of S_{max}. Rose

diagrams show the distribution of S_{Hmax} orientation in zones where active faulting occurs (i.e., strain rate ≥ 10^{-16} s^{-1}). Large

grey arrows for the y-seed configuration mark the change from a symmetric to an asymmetric S_{Hmax} distribution.

3.7.1. Effect of S_{Hmax} re-orientation on rift propagation of competing rift segments (v-seed models)

Early stages in our numerical experiments are characterized by rift deflection and curved fault traces in the model center where rift segments interact (see Fig. 6). Hereafter, we refer to that phenomenon as arcuate faulting. Arcuate faulting mainly occurs in experiments with larger intermediate angles (>10°) in early stages (Fig. 6), especially if two competing rift segments are present (v-, and y-seed configurations). Moreover, we have shown that deflection of propagating rifts occurs when deformation is symmetrically distributed along both competing rift branches. This is clearly visible for the v-seed configuration (Fig. 8a-e). Assuming orthogonal extension and isotropic material properties, S_{Hmax} is expected to align perpendicular to the extension direction producing pure dip-slip normal faults (Anderson, 1905). However, the model shows an immediate S_{Hmax} re-orientation at early deformation stages (i.e., after 0.4 million years; Fig. 8a) from a N-S to a E-W orientation in the vicinity of the underlying weak seeds such that dip slip faults are favored over oblique-slip faults with a strike-slip component. With progressive extension (Fig. 8b-e), S_{Hmax} re-orientations successively propagate into the isotropic zone without pre-existing structures, concomitant with the rift propagation. Consequently, the position of the front where stress rotation occurs propagates over time resulting in the deflection of the propagating rift arms away from each other.

518 There is a distinct difference between stress deflection along weak structures and E-W

519 deflections of S_{Hmax} in zones where strain rates are below the set threshold of 10^{-16} s^{-1}. The v-

520 seed configuration shows localized strain accumulation along one rift boundary fault per

521 segment (i.e., the outer one) resulting in a rift zone with a broad graben system that subsides

522 (Fig. 8e). S_{Hmax} re-orientation inside of the graben is in parts identical to the E-W orientation

523 of S_{Hmax} outside of the graben. While local S_{Hmax} rotations may be explained by small

524 differences in the maximum and intermediate principal stress components, such E-W stress

525 re-orientation in our model occurs systematically and suggest that this feature reflects the

526 influence of the strength anisotropy (Morley, 2010). The initial S_{Hmax} deflection near weak

527 structures locally favors dip-slip faulting but also has regional influence on the overall stress

528 regime.

529

530 **3.7.2. S_{Hmax} evolution in sub-parallel rift segments (i-seed models)**

531 During the early stage (i.e., after 0.4 million years, Fig. 8f), the distribution of S_{Hmax} resembles

532 the distribution from the v-seed configuration described in the previous section. Stress

533 deflection mainly occurs in zones where a weak fabric is present. S_{Hmax} values in the central

534 zone rotate by a small amount and reflect arcuate faulting (see Fig. 6). Since the two rift

535 segments propagate in opposing directions, linkage is efficient and localizes in a short time

536 (Fig. 8f-j). S_{Hmax} values deflect accordingly along propagating faults, which affects the entire

537 model domain. This deflection does not occur symmetrically on both sides of each rift segment.

538 Rather, it shows two distinct zones: 1) E-W orientations outside the rift deflect into a parallel

539 orientation near the rift boarder or 2) N-S orientations outside of the rift deflect into E-W

540 orientations near faults (Fig. 8j).

541

542 We find that S_{Hmax} orientations deflect gradually from E-W to N-S along abandoned rift

543 boundary faults where activity ceased (Fig. 8h-j; upper left and lower right model domain). In

544 contrast, S_{Hmax} re-orientations from N-S to nearly E-W towards active rift boundary faults are

545 followed by a rapid flip back to N-S along the faults (Fig. 8h-j; lower left and upper right model

546 domain). The two types of re-orientation seem to correspond with two types of deformed

547 zones. Where deformation is strongly localized along rift boundary faults, jumps in the S_{Hmax}

548 orientation occur. In contrast, zones where inward migration of fault activity activates intra-

549 rift faults, S_{Hmax} re-orientation occurs gradually.

550

551 ### 3.7.3. Rift arm competition and deflection (y-seed models)

552 A prominent feature in our models with two competing rift segments is the deflection of rift

553 branches and arcuate strain rate patterns (Fig. 8a-e) in the model with a v-seed configuration.

554 Moreover, the i-seed configuration demonstrates a gradual S_{Hmax} re-orientation over a broader

555 pre-weakened zone due to formerly active boundary faults. One could therefore expect that

556 both features should occur in the model with y-seed configuration (Fig. 8k-o).

557

558 Indeed, early stages (i.e., after 0.4 million years; Fig. 8k) are characterized by a symmetric

559 stress field with re-oriented S_{Hmax} values near the two rear rift segments. However, in contrast

560 to the v-seed configuration, S_{Hmax} re-orientation also occurs near the frontal pre-existing weak

561 fabric along developing rift boundary faults. In the isotropic zone, S_{Hmax} values dominantly

562 show a N-S direction. The general N-S orientation reflects the regional stress field due to an

563 E-W extension as predicted by Anderson (1905) in isotropic areas, into which rift segments

564 have yet to propagate. With ongoing extension, all three rift segments propagate into the

565 isotropic zone and cause a re-orientation of S_{Hmax} (Fig. 8l). Note that after 0.8 million years

566 the stress re-orientation occurs symmetrically. This contrasts with the i-seed configuration

567 where S_{Hmax} values deflect into either an E-W orientation along active rift boundary faults or

568 gradually turn into a fault parallel direction over a broader weakened zone (see subsection

569 3.7.2.). The early symmetric stress distribution in the y-seed configuration model is

570 unarguably due to the symmetric seed configuration (see also Fig. 8a-e). At this stage, dip-

571 slip faulting along the competing sub-parallel rift segments is favored over oblique slip faults

572 as in models with a v-seed configuration. It is only after 1.2 million years, when fault activity

573 along the right rear segment ceases that deformation localizes along the left rear and frontal

574 segments and linkage intensifies (Fig. 8m). Successively, localization and linkage occur

575 coevally with a switch from a symmetric to an asymmetric stress distribution and resembles

576 more the stress distribution in the i-seed configuration model (Fig. 8f-j). The model state after

577 1.2 million years (Fig. 8m) also marks the switch from a symmetric to an asymmetric stress

578 distribution that was formerly dominated by the competing rear rift segments with dip-slip

579 faulting favored along the two competing rift segments (see also v-seed configuration; Fig. 8

580 a-e). After 1.2 million years the system is dominated by the linkage of two obliquely oriented

581 segments (i.e., i-seed configuration). Note that after 1.2 million years dip-slip faulting mostly

582 occurs along the competing rift segment that links with the opposingly propagating segment

583 whereas dominantly oblique slip faults occur along the abandoned rift segment where activity

584 ceases.

585

586 The symmetry switch is also visible in rose diagrams of stress orientations within the active

587 faulting zone (i.e., strain rate $\geq 10^{-16}$ s^{-1}). A dominantly N-S oriented S_{Hmax} distribution changes

588 to a bimodal distribution with a second E-W orientation (Fig. 8l-n). Similarly, bimodal S_{Hmax}

589 distribution is also visible in the experiment with an i-seed configuration but occurs earlier.

590 Since the experiment with an i-seed configuration is never in the state of an early symmetric

591 stress distribution linkage is facilitated and occurs earlier (Fig.8g-i).

592

4. Discussion

594 Despite the relatively simple setup of our experiments, the interaction of individual weak seeds

595 generates a complex evolution of linkage patterns. In the following we discuss the effect of

596   pre-existing structures on S_{Hmax} re-orientations and how, in return, stress re-orientation

597   influences rift propagation and rift segment linkage.

598

4.1.   Effect of pre-existing structures on rift segment propagation, interaction, and S_{Hmax}

601   Previous modelling studies demonstrated that pre-existing weaknesses may cause local re-

602   orientations of S_{Hmax} resulting in extensional faults with an oblique orientation to the regional

603   extension direction which exhibit pure dip-slip behavior (e.g., Morley, 2010; Corti et al., 2013;

604   Morley, 2017; Philippon et al., 2015). This contrasts the expected (assuming Andersonian

605   faulting theory) occurrence of faults with an oblique slip component above pre-existing

606   structures that are obliquely oriented with respect to the extension direction (Tron and Brun,

607   1991; Withjack and Jamison, 1986). Our S_{Hmax} analysis documents two types of stress re-

608   orientation, either gradually or by a jump along faults (Fig. 8i). A potential explanation for the

609   two types of stress deflection is that cessation of boundary fault activity (and subsequent

610   faulting activity along intra-rift faults) creates a broad zone of reduced crustal strength. Hence,

611   S_{Hmax} orientations successively re-orient along those formerly active faults and eventually

612   rotate into a N-S orientation along active intra-rift faults. In contrast, where faulting activity

613   is strongly localized along rift boundary faults, re-orientation occurs rapidly by a jump from E-

614   W to a N-S orientation. This suggests that formerly active faults act as a wider zone of pre-

615   weakened material, where stresses deflect sequentially rather than with a rapid jump. Similar

616   observations have been made in previous studies of numerical models (Gudmundsson et al.,

617   2010; Kattenhorn et al., 2000). These experiments suggest that earlier fractures lead to

618   subzones (within a broader damage zone), where stresses subsequently rotate away from the

619   regional stress field. Although our analog and numerical models do not feature elastic

620   deformation, they indicate that stress deflection is an ongoing process, even after elastic

621   material failure. Such a stress deflection further implies that stress orientations in rocks with

622 pre-existing weaknesses can substantially deviate from predicted orientations in isotropic

623 media (Anderson, 1905).

624

625 It has been proposed that early faulting and propagation in the Rukwa and North Malawi Rifts

626 (Fig. 1c) were guided by pre-existing basement fabrics (Heilman et al., 2019). This region is

627 further shaped by a flip in the boundary fault polarity in the present-day geometry within the

628 interaction zone between Rukwa Rift and North Malawi Rift (Bosworth, 1985). Our i-seed

629 models show identical geometries for increasing intermediate angles (Figs. 7h,i and S5), where

630 plastic strain near pre-existing structures is mostly accommodated along prominent rift

631 boundary faults that flip fault polarity from the frontal to the rear rift segment. This flip in

632 fault polarity occurs prominently in models with an intermediate angle $\geq 10°$. We speculate

633 that the increasing obliquity of the southward propagating rift segment favors asymmetric

634 graben evolution with one dominant boundary fault accommodating a larger amount of strain.

635 In contrast to small intermediate angles (i.e., $10°$), seed configurations with a higher obliquity

636 provoke local rotation of S_{Hmax} within the interaction zone into a strike-slip regime near the

637 subordinate boundary fault (Fig. S5). Hence, strain accommodation along incipient faults

638 within the dip-slip regime is favored. This facilitates propagation along those dominant rift

639 boundary faults and eventually defines the final rift geometry.

640

641 Kolawole et al. (2018) further propose two different types of strain accommodation at early

642 rift phases. Prominent strain accommodation localized onto a discrete and narrow zone along

643 large rift boundary faults (Style-1; sensu Kolawole et al., 2018) and faulting distributed over

644 a broader zone, where fault clusters may reflect pre-conditioning of the material (Style-2;

645 sensu Kolawole et al., 2018). With this perspective, jumps and gradual rotation of S_{Hmax}

646 orientations are comparable to Style-1 and Style-2 strain localization, respectively, as

647 proposed by Kolawole et al. (2018). Hence, the type of weakness (narrow discrete zone or

648 distributed cluster zone) should also be reflected by the stress re-orientation distribution

649 (Morley, 2010).

650

4.2. Local S_{Hmax} re-orientation and its influence on rift segment interaction

651

652 **and rift deflection**

653 A particular observation in our experiments with a v-, and y-seed configuration is that two

654 sub-parallel rift segments, which propagate approximately in the same direction deflect away

655 from each other at early stages. This is somewhat surprising as one would expect the two rift

656 segments to cut towards each other by minimizing fault length. The occurrence of rift

657 deflection in both analog and numerical experiments validates that the results are robust and

658 require discussing the role of S_{Hmax} re-orientation and how it influences rift segment

659 interaction.

660

661 We speculate that, while both rear rift segments in our y-seed models equivalently

662 accommodate strain in the early stages (i.e., when the overall stress distribution is symmetric;

663 Fig. 8), S_{Hmax} orientations are dominated by the influence of the two competing rear rift

664 segments that accommodate strain in equal parts. It is only after fault activity along one rear

665 segment ceases that deformation localizes along the active rear and frontal segments and

666 linkage intensifies. Strain localization and linkage occur coevally with a switch from a

667 symmetric to an asymmetric stress distribution resembling the stress distributions in v-, and

668 i-seed configuration models, respectively. The switch from a symmetric to an asymmetric

669 stress distribution in y-seed models also marks the switch from a system that was formerly

670 dominated by the competing rear rift segments (i.e., v-seed configuration) to a system that

671 is dominated by the linkage of two obliquely oriented segments (i.e., i-seed configuration).

672

673   In models with a v-seed configuration, however, the symmetric phase prevails and causes

674   coeval S_{Hmax} re-orientations and rift deflection that cause divergence of the two propagating

675   rift segments. A similar process of extensional segment interaction via stress rotation is known

676   from mid-ocean ridge settings: Pollard and Aydin (1984) argue that paths of two opposingly

677   propagating oceanic ridges weakly diverge due to shear stresses that divert propagating ridges

678   as they approach each other. Once the two ridges overlap, the stress field changes causing

679   convergence and intersection. Similarly, Nelson et al. (1992) describe interference of

680   compressional zones of propagating cracks diverting their tips before they overlap and turn

681   back toward another. In this respect, our models with a v-seed configuration suggest that

682   stresses also cause divergence of two rift segments that propagate approximately in the same

683   direction. However, overlap never occurs (as they propagate approximately in the same

684   direction) and hence, the two segments remain in a stress field that further diverts their paths.

685

686   Only in models with a y-seed configuration, compressional zones and rift deflection can be

687   overcome once the opposingly propagating rift segment links with one of the competing rift

688   segments. Linkage occurs after about the first million years, concurrently with rift deflection

689   and abandonment of the right rear segment (Figs. 9a and S6). Moreover, remaining activity

690   in the right rear segment depicts low strain rates along numerous arcuate intra-rift faults (Figs.

691   9b and S6). This suggests that linkage and rift abandonment are closely coupled and faulting

692   along the linked segments intensifies when the activity along the remaining rift segment

693   ceases. In addition, the left rear segment displays a rather asymmetric half graben geometry

694   (Figs. 5c,d, 7i and S4) with one prominent rift boundary fault accommodating a larger part of

695   plastic strain similar to our models with a i-seed configuration (see also Figs. 7e,f and S5).

696   Dominant strain accommodation occurs along the west-dipping rift boundary fault of the left

697   rear segment coinciding with jumps in the S_{Hmax} orientation (Fig. 8m-o). Our modelling results

698   show that stress deflection along rift segment tips is a mechanical consequence of the

699   interaction between weak zones and far-field stresses offering a potential explanation for

700   naturally occurring rift deflection. However, we must emphasize that complexities in natural

701   rift settings pose additional difficulties that require further investigations of stress orientations.

702

703   An example of rift deflection in nature has been described in the Main Ethiopian Rift.

704   Geophysical and geologic studies evidence that pre-existing structures controlled the

705   approximately 11 Ma southward propagation of the Northern Main Ethiopian Rift and its

706   contemporaneous westward deflection along the Yerer-Tullu Wellel Volcanotectonic

707   Lineament (YTVL; Abebe et al., 1998; Keranen and Klemperer, 2008; Muhabaw et al., 2022).

708   Only after the rotation of the principal stress direction at about 5-6 Ma (Bonini et al., 2005),

709   extension along the YTVL ceased and deformation localization along the Central Main

710   Ethiopian Rift became more favorable. Our models document similar rift deflections and

711   moreover indicate that, even in the absence of changing plate motions, rift segments deflect,

712   and may cease while competing rift segments prevail and strain further localizes.

713

714   For the Canyonlands National Park, it has been proposed that it is mainly the lateral offset

715   between pre-existing structures that explains the diversity of structures (Allken et al., 2013;

716   Fig. 1d). With larger offsets, interaction between adjacent rift segments is limited and

717   competing grabens persist and endure ongoing propagation coevally. We find that stresses,

718   in combination with the geometry of pre-existing structures, play an important role and that

719   they have a mutual effect on one another. Hence, stress distribution must be considered as

720   an important factor especially in early rifting stages when segments link and predetermine

721   strain localization during subsequent progressive rifting.

722
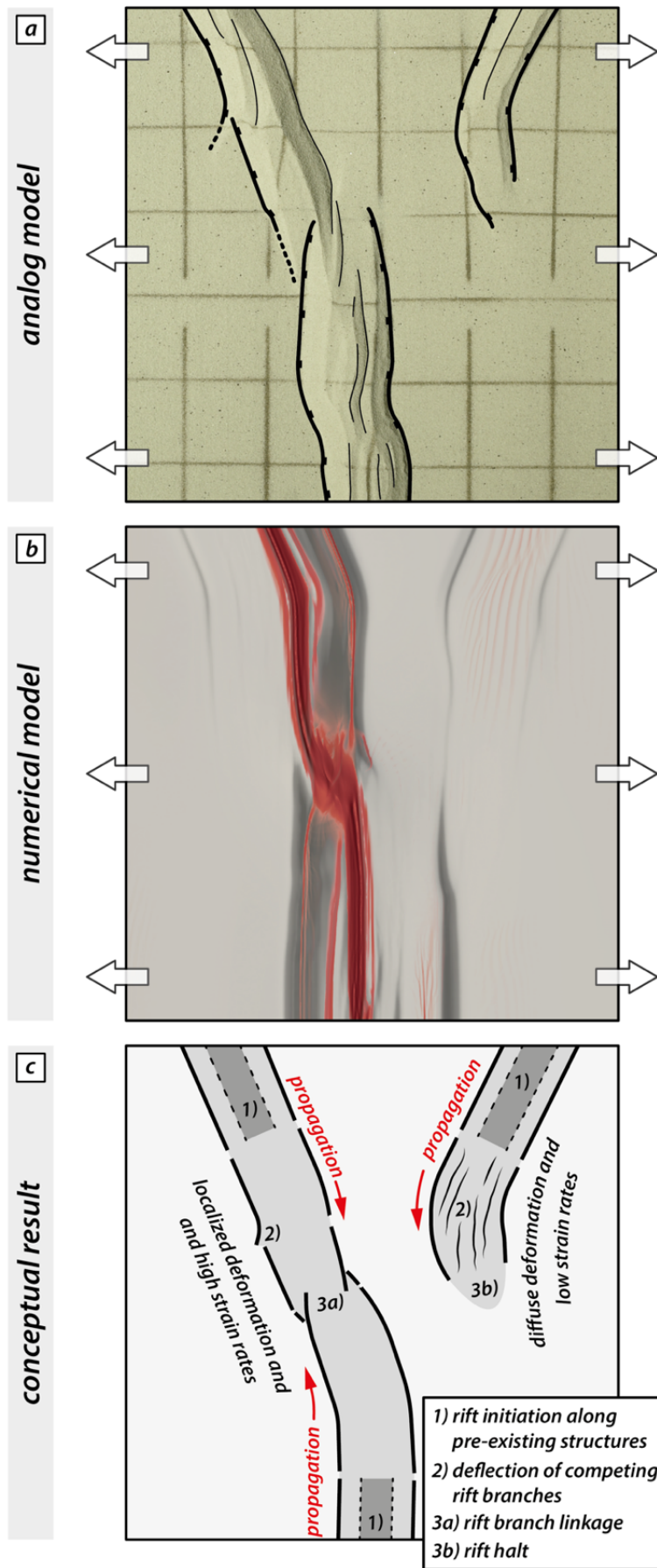
Figure 9: *Summary plot showing the geometric similarity of rift segment linkage, deflection of competing branches and abandonment in analog and numerical models. a) Observed key features at the final stage of the analog model. b) Final strain and strain rate pattern in the numerical reference model. c) Conceptual interpretation of rift deflection and linkage based on our analog and numerical results (for details see text).*

723

5. Conclusions

We present a series of analog and numerical rifting experiments. Our results suggest that, even in a relatively simple iso-viscous two-layer crustal setup, pre-existing weaknesses substantially disturb the regional stress pattern, which impacts rift propagation and the overall rift evolution. The complex stress re-orientation is distinct for different seed configurations (i.e., v-seed, i-seed, and y-seed) and closely interacts with the final rift geometry. The most important findings of our study can be summarized as follows:

- Our numerical experiments reproduce rift segment deflection seen in our analog models. This highlights the robustness of our results and their applicability to interpreting rift segment propagation, interaction, and linkage in natural settings of continental rifting.

- Pre-existing structures may control localization of rift segments that successively propagate into previously undeformed areas. Consequently, stress re-orientation initially occurs along pre-conditioned zones and propagates, coevally with rift segment propagation and strain accrual, into formerly undeformed areas.

- Interacting stresses between two competing rift segments may cause outward deflection of the propagating rift tips resulting in a successively broader rift geometry along-strike.

- Outward deflection of competing rift segments is less prominent if an opposingly propagating rift segment is present. With progressive extensional deformation, strain accrual along one of the competing rift segments prevails whilst faulting activity along the other segment ceases. Coevally, the general stress orientation changes from a symmetric to an asymmetric distribution indicating the onset of rift linkage.

- Our modelling results reproduce first-order structures of natural examples from the East African Rift System and, on smaller scale, graben structures in the Canyonlands

750   National Park. The combined investigation of surface stresses and strain localization

751   provides an explanation for distinct rift deflection among competing rift segments and

752   rift linkage structures where ongoing deformation and stresses mutually affect each

753   other.

754

755 While changes in rift orientation are often used to infer changes in plate-motion, we

756 demonstrate that local stress field re-orientations can occur under constant plate motions.

757 Albeit on a smaller scale, implications from our observations corroborate findings from

758 previous studies (Brune; 2014; Duclaux et al., 2020; Gapais et al., 2000). Locally, stress and

759 strain can largely deviate from a regional, far-field pattern and instead represent local

760 deformation interference. In addition, the observed stress re-orientations change over time

761 indicating that stresses measured in natural examples may depict transient stages that change

762 with progressive deformation due to subsequent changes in material strengths (Morley et al.,

763 2004). This implication must be considered in processing local fault-slip data when interpreting

764 the evolution of rifts at any scale.

765

766 ## Data availability

767 Rheological measurements of the used analog materials are available in the form of open

768 access data publications provided by the GFZ Data Service (brittle materials: Schmid et al.,

769 2020a; Schmid et al., 2020b; viscous materials: Zwaan et al., 2018). The input files, custom

770 ASPECT plugins and post processing scripts used in this publication can be found in Zenodo

771 repository https://zenodo.org/badge/latestdoi/610197324 (Glerum; 2023).

772

773

774

775

Acknowledgements

We thank Esther Heckenbach for helpful assistance with post processing and visualization. The work was supported by the North-German Supercomputing Alliance (HLRN). We thank the Swiss National Science Foundation for providing financial support. Finally, we thank the two Referees, Guillaume Duclaux and Chris Morley as well as Topical Editor Patrice Rey for their detailed, constructive and motivating comments that significantly helped to improve this manuscript.

Funding

This project is supported by the Swiss National Science Foundation [grant number 200021_178731].

CRediT authorship contribution statement

Timothy C. Schmid: Conceptualization, Methodology, Investigation, Formal Analysis, Writing – original draft, Visualization, Data curation. Sascha Brune: Conceptualization, Methodology, HPC funding acquisition, Supervision, Project administration, Writing – review & editing. Anne Glerum: Methodology, Software, HPC funding acquisition, Writing – review & editing. Guido Schreurs: Writing – review & editing, Supervision, Project administration, Funding acquisitions, Resources.

References

Abebe, T., Mazzarini, F., Innocenti, F., and Manetti, P.: The Yerer-Tullu Wellel volcanotectonic lineament: A transtensional structure in central Ethiopia and the associated magmatic activity, Journal of African Earth Sciences, 26, 135-150, 1998.
https://doi.org/10.1016/S0899-5362(97)00141-3

Acocella, V., Faccenna, C., Funiciello, R., and Rossetti, F.: Sand-box modelling of basement-controlled transfer zones in extensional domains, Terra Nova-Oxford, 11, 149-156, 1999.

Adam, J., Urai, J., Wieneke, B., Oncken, O., Pfeiffer, K., Kukowski, N., Lohrmann, J., Hoth, S., Van Der Zee, W., and Schmatz, J.: Shear localisation and strain distribution during tectonic faulting—New insights from granular-flow experiments and high-resolution optical image correlation techniques, Journal of Structural Geology, 27, 283-301, 2005.
https://doi.org/10.1016/j.jsg.2004.08.008

Allken, V., Huismans, R. S., and Thieulot, C.: Three-dimensional numerical modeling of upper crustal extensional systems, Journal of Geophysical Research: Solid Earth, 116, 2011.
https://doi.org/10.1029/2011JB008319

Allken, V., Huismans, R. S., and Thieulot, C.: Factors controlling the mode of rift interaction in brittle-ductile coupled systems: A 3D numerical study, Geochemistry, Geophysics, Geosystems, 13, 2012.
https://doi.org/10.1029/2012GC004077

Allken, V., Huismans, R. S., Fossen, H., and Thieulot, C.: 3D numerical modelling of graben interaction and linkage: a case study of the Canyonlands grabens, Utah, Basin Research, 25, 436-449, 2013.
https://doi.org/10.1111/bre.12010

Anderson, E. M.: The dynamics of faulting, Transactions of the Edinburgh Geological Society, 8, 387-402, 1905.
https://doi.org/10.1144/transed.8.3.387

Bellahsen, N. and Daniel, J. M.: Fault reactivation control on normal fault growth: an experimental study, Journal of Structural Geology, 27, 769-780, 2005.
https://doi.org/10.1016/j.jsg.2004.12.003

Bonini, M., Corti, G., Innocenti, F., Manetti, P., Mazzarini, F., Abebe, T., and Pecskay, Z.: Evolution of the Main Ethiopian Rift in the frame of Afar and Kenya rifts propagation, Tectonics, 24, 2005.
https://doi.org/10.1029/2004TC001680

Bosworth, W.: Geometry of propagating continental rifts, Nature, 316, 625-627, 1985.
https://doi.org/10.1038/316625a0

Brune, S.: Evolution of stress and fault patterns in oblique rift systems: 3-D numerical lithospheric-scale experiments from rift to breakup, Geochemistry, Geophysics, Geosystems, 15, 3392-3415, 2014.
https://doi.org/10.1002/2014GC005446

Brune, S. and Autin, J.: The rift to break-up evolution of the Gulf of Aden: Insights from 3D numerical lithospheric-scale modelling, Tectonophysics, 607, 65-79, 10.1016/j.tecto.2013.06.029, 2013.
https://doi.org/10.1016/j.tecto.2013.06.029

Brune, S., Corti, G., and Ranalli, G.: Controls of inherited lithospheric heterogeneity on rift linkage: Numerical and analog models of interaction between the Kenyan and Ethiopian rifts across the Turkana depression, Tectonics, 36, 1767-1786, 2017.
https://doi.org/10.1002/2017TC004739

Brune, S., Popov, A. A., and Sobolev, S. V.: Modeling suggests that oblique extension facilitates rifting and continental break-up, Journal of Geophysical Research: Solid Earth, 117, 2012.
https://doi.org/10.1029/2011JB008860

Childs, C., Watterson, J., and Walsh, J.: Fault overlap zones within developing normal fault systems, Journal of the Geological Society, 152, 535-549, 1995.
https://doi.org/10.1144/gsjgs.152.3.0535

858 Collanega, L., Jackson, C. A.-L., Bell, R., Coleman, A. J., Lenhart, A., and Breda, A.: How do intra-basement fabrics
859 influence normal fault growth? Insights from the Taranaki Basin, offshore New Zealand, 2018.
860 https://doi.org/10.31223/osf.io/8rn9u
861
862 Corti, G.: Evolution and characteristics of continental rifting: Analog modeling-inspired view and comparison with
863 examples from the East African Rift System, Tectonophysics, 522-523, 1-33, 10.1016/j.tecto.2011.06.010, 2012.
864 https://doi.org/10.1016/j.tecto.2011.06.010
865
866 Corti, G., van Wijk, J., Cloetingh, S., and Morley, C. K.: Tectonic inheritance and continental rift architecture:
867 Numerical and analogue models of the East African Rift system, Tectonics, 26, 2007.
868 https://doi.org/10.1029/2006TC002086
869
870 Corti, G., Philippon, M., Sani, F., Keir, D., and Kidane, T.: Re-orientation of the extension direction and pure
871 extensional faulting at oblique rift margins: Comparison between the Main Ethiopian Rift and laboratory
872 experiments, Terra Nova, 25, 396-404, 2013.
873 https://doi.org/10.1111/ter.12049
874
875 Corti, G., Cioni, R., Franceschini, Z., Sani, F., Scaillet, S., Molin, P., Isola, I., Mazzarini, F., Brune, S., and Keir, D.:
876 Aborted propagation of the Ethiopian rift caused by linkage with the Kenyan rift, Nature communications, 10, 1-
877 11, 2019.
878 https://doi.org/10.1038/s41467-019-09335-2
879
880 Crameri, F., Shephard, G. E., and Heron, P. J.: The misuse of colour in science communication, Nature
881 communications, 11, 1-10, 2020.
882 https://doi.org/10.1038/s41467-020-19160-7
883
884 Daly, M., Chorowicz, J., and Fairhead, J.: Rift basin evolution in Africa: the influence of reactivated steep basement
885 shear zones, Geological Society, London, Special Publications, 44, 309-334, 1989.
886 https://doi.org/10.1144/GSL.SP.1989.044.01.17
887
888 Duclaux, G., Huismans, R. S., and May, D. A.: Rotation, narrowing, and preferential reactivation of brittle structures
889 during oblique rifting, Earth and Planetary Science Letters, 531, 115952, 2020.
890 https://doi.org/10.1016/j.epsl.2019.115952
891
892 Duffy, O. B., Bell, R. E., Jackson, C. A.-L., Gawthorpe, R. L., and Whipp, P. S.: Fault growth and interactions in a
893 multiphase rift fault network: Horda Platform, Norwegian North Sea, Journal of Structural Geology, 80, 99-119,
894 2015.
895 https://doi.org/10.1016/j.jsg.2015.08.015
896
897 Duretz, T., de Borst, R., and Le Pourhiet, L.: Finite thickness of shear bands in frictional viscoplasticity and
898 implications for lithosphere dynamics, Geochemistry, Geophysics, Geosystems, 20, 5598-5616, 2019.
899 https://doi.org/10.1029/2019GC008531
900
901 Ebinger, C., Yemane, T., Harding, D., Tesfaye, S., Kelley, S., and Rex, D.: Rift deflection, migration, and
902 propagation: Linkage of the Ethiopian and Eastern rifts, Africa, Geological Society of America Bulletin, 112, 163-
903 176, 2000.
904 https://doi.org/10.1130/0016-7606(2000)112<163:RDMAPL>2.0.CO;2
905
906 Gapais, D., Cobbold, P. R., Bourgeois, O., Rouby, D., and de Urreiztieta, M.: Tectonic significance of fault-slip data,
907 Journal of Structural Geology, 22, 881-888, 2000.
908 https://doi.org/10.1016/S0191-8141(00)00015-8
909
910 Gassmöller, R., Lokavarapu, H., Heien, E., Puckett, E. G., and Bangerth, W.: Flexible and scalable particle-in-cell
911 methods with adaptive mesh refinement for geodynamic computations, Geochemistry, Geophysics, Geosystems,
912 19, 3596-3604, 2018.
913 https://doi.org/10.1029/2018GC007508
914
915 Glerum, A., Brune, S., Stamps, D. S., and Strecker, M. R.: Victoria continental microplate dynamics controlled by
916 the lithospheric strength distribution of the East African Rift, Nature Communications, 11, 1-15, 2020.
917 https://doi.org/10.1038/s41467-020-16176-x
918
919 Glerum, A., Thieulot, C., Fraters, M., Blom, C., and Spakman, W.: Nonlinear viscoplasticity in ASPECT:
920 benchmarking and applications to subduction, Solid Earth, 9, 267-294, 2018.
921 https://doi.org/10.5194/se-9-267-2018

922 Glerum, A.: anne-glerum/paper-Schmid-Tectonic-interactions-during-rift-linkage: Update ASPECT branch
923 (v.2.0.0). Zenodo, 2023.
924 https://doi.org/10.5281/zenodo.7701374

926 Gudmundsson, A., Simmenes, T. H., Larsen, B., and Philipp, S. L.: Effects of internal structure and local stresses
927 on fracture propagation, deflection, and arrest in fault zones, Journal of Structural Geology, 32, 1643-1655, 2010.
928 https://doi.org/10.1016/j.jsg.2009.08.013

930 Heidbach, O., Rajabi, M., Cui, X., Fuchs, K., Müller, B., Reinecker, J., Reiter, K., Tingay, M., Wenzel, F., and Xie,
931 F.: The World Stress Map database release 2016: Crustal stress pattern across scales, Tectonophysics, 744, 484-
932 498, 2018.
933 https://doi.org/10.1016/j.tecto.2018.07.007

935 Heilman, E., Kolawole, F., Atekwana, E. A., and Mayle, M.: Controls of Basement Fabric on the Linkage of Rift
936 Segments, Tectonics, 38, 1337-1366, 10.1029/2018tc005362, 2019.
937 https://doi.org/10.1029/2018TC005362

939 Heister, T., Dannberg, J., Gassmöller, R., and Bangerth, W.: High accuracy mantle convection simulation through
940 modern numerical methods–II: realistic models and problems, Geophysical Journal International, 210, 833-851,
941 2017.
942 https://doi.org/10.1029/2018TC005362

944 Jacquey, A. B. and Cacace, M.: Multiphysics modeling of a brittle-ductile lithosphere: 2. Semi-brittle, semi-ductile
945 deformation and damage rheology, Journal of Geophysical Research: Solid Earth, 125, e2019JB018475, 2020.
946 https://doi.org/10.1029/2019JB018475

948 Kattenhorn, S. A., Aydin, A., and Pollard, D. D.: Joints at high angles to normal fault strike: an explanation using
949 3-D numerical models of fault-perturbed stress fields, Journal of structural Geology, 22, 1-23, 2000.
950 https://doi.org/10.1016/S0191-8141(99)00130-3

952 Katzman, R., ten Brink, U. S., and Lin, J.: Three-dimensional modeling of pull-apart basins: Implications for the
953 tectonics of the Dead Sea Basin, Journal of Geophysical Research: Solid Earth, 100, 6295-6312, 1995.
954 https://doi.org/10.1029/94JB03101

956 Keranen, K. and Klemperer, S.: Discontinuous and diachronous evolution of the Main Ethiopian Rift: Implications
957 for development of continental rifts, Earth and Planetary Science Letters, 265, 96-111, 2008.
958 https://doi.org/10.1016/j.epsl.2007.09.038

960 Koehn, D., Aanyu, K., Haines, S., and Sachau, T.: Rift nucleation, rift propagation and the creation of basement
961 micro-plates within active rifts, Tectonophysics, 458, 105-116, 2008.
962 https://doi.org/10.1016/j.tecto.2007.10.003

964 Kolawole, F., Phillips, T. B., Atekwana, E. A., and Jackson, C. A.-L.: Structural inheritance controls strain distribution
965 during early continental rifting, rukwa rift, Frontiers in Earth Science, 670, 2021.
966 https://doi.org/10.3389/feart.2021.707869

968 Kolawole, F., Atekwana, E. A., Laó-Dávila, D. A., Abdelsalam, M. G., Chindandali, P. R., Salima, J., and Kalindekafe,
969 L.: Active Deformation of Malawi Rift's North Basin Hinge Zone Modulated by Reactivation of Preexisting
970 Precambrian Shear Zone Fabric, Tectonics, 37, 683-704, 10.1002/2017tc004628, 2018.
971 https://doi.org/10.1002/2017TC004628

973 Kronbichler, M., Heister, T., and Bangerth, W.: High accuracy mantle convection simulation through modern
974 numerical methods, Geophysical Journal International, 191, 12-29, 2012.
975 https://doi.org/10.1111/j.1365-246X.2012.05609.x

977 Lavier, L. L., Buck, W. R., and Poliakov, A. N.: Factors controlling normal fault offset in an ideal brittle layer, Journal
978 of Geophysical Research: Solid Earth, 105, 23431-23442, 2000.
979 https://doi.org/10.1029/2000JB900108

981 Macdonald, K. C. and Fox, P.: Overlapping spreading centres: New accretion geometry on the East Pacific Rise,
982 Nature, 302, 55-58, 1983.
983 https://doi.org/10.1038/302055a0

985 Mills, N.: Dislocation array elements for the analysis of crack and yielded zone growth, Journal of Materials Science,
986 16, 1317-1331, 1981.
987 https://doi.org/10.1007/BF01033848
988
989 Mondy, L. S., Rey, P. F., Duclaux, G., and Moresi, L.: The role of asthenospheric flow during rift propagation and
990 breakup, Geology, 46, 103-106, 2018.
991 https://doi.org/10.1130/G39674.1
992
993 Morley, C.: Stress re-orientation along zones of weak fabrics in rifts: An explanation for pure extension in 'oblique'
994 rift segments?, Earth and Planetary Science Letters, 297, 667-673, 2010.
995 https://doi.org/10.1016/j.epsl.2010.07.022
996
997 Morley, C.: The impact of multiple extension events, stress rotation and inherited fabrics on normal fault geometries
998 and evolution in the Cenozoic rift basins of Thailand, Geological Society, London, Special Publications, 439, 413-
999 445, 2017.
1000 https://doi.org/10.1144/SP439.3
1001
1002 Morley, C., Nelson, R., Patton, T., and Munn, S.: Transfer zones in the East African rift system and their relevance
1003 to hydrocarbon exploration in rifts, AAPG bulletin, 74, 1234-1253, 1990.
1004 https://doi.org/10.1306/0C9B2475-1710-11D7-8645000102C1865D
1005
1006 Morley, C., Haranya, C., Phoosongsee, W., Pongwapee, S., Kornsawan, A., and Wonganan, N.: Activation of rift
1007 oblique and rift parallel pre-existing fabrics during extension and their effect on deformation style: examples from
1008 the rifts of Thailand, Journal of Structural Geology, 26, 1803-1829, 2004.
1009 https://doi.org/10.1016/j.jsg.2004.02.014
1010
1011 Morley, C. K.: Patterns of displacement along large normal faults: implications for basin evolution and fault
1012 propagation, based on examples from East Africa, AAPG bulletin, 83, 613-634, 1999.
1013 https://doi.org/10.1306/00AA9C0A-1730-11D7-8645000102C1865D
1014
1015 Muhabaw, Y., Muluneh, A. A., Nugsse, K., Gebru, E. F., and Kidane, T.: Paleomagnetism of Gedemsa magmatic
1016 segment, Main Ethiopian Rift: Implication for clockwise rotation of the segment in the Early Pleistocene,
1017 Tectonophysics, 838, 229475, 2022.
1018 https://doi.org/10.1016/j.tecto.2022.229475
1019
1020 Nelson, R., Patton, T., and Morley, C.: Rift-segment interaction and its relation to hydrocarbon exploration in
1021 continental rift systems, AAPG bulletin, 76, 1153-1169, 1992.
1022 https://doi.org/10.1306/BDFF898E-1718-11D7-8645000102C1865D
1023
1024 Oliva, S. J., Ebinger, C. J., Rivalta, E., Williams, C. A., Wauthier, C., and Currie, C. A.: State of stress and stress
1025 rotations: Quantifying the role of surface topography and subsurface density contrasts in magmatic rift zones
1026 (Eastern Rift, Africa), Earth and Planetary Science Letters, 584, 117478, 2022.
1027 https://doi.org/10.1016/j.epsl.2022.117478
1028
1029 Philippon, M., Willingshofer, E., Sokoutis, D., Corti, G., Sani, F., Bonini, M., and Cloetingh, S.: Slip re-orientation in
1030 oblique rifts, Geology, 43, 147-150, 2015.
1031 https://doi.org/10.1130/G36208.1
1032
1033 Pollard, D. D. and Aydin, A.: Propagation and linkage of oceanic ridge segments, Journal of Geophysical Research:
1034 Solid Earth, 89, 10017-10028, 1984.
1035 https://doi.org/10.1029/JB089iB12p10017
1036
1037 Rose, I., Buffett, B., and Heister, T.: Stability and accuracy of free surface time integration in viscous flows, Physics
1038 of the Earth and Planetary Interiors, 262, 90-100, 2017.
1039 https://doi.org/10.1016/j.pepi.2016.11.007
1040
1041 Rosendahl, B. R.: Architecture of continental rifts with special reference to East Africa, Annual Review of Earth and
1042 Planetary Sciences, 15, 445, 1987.
1043 https://doi.org/10.1146/annurev.ea.15.050187.002305
1044
1045 Saria, E., Calais, E., Stamps, D., Delvaux, D., and Hartnady, C.: Present-day kinematics of the East African Rift,
1046 Journal of Geophysical Research: Solid Earth, 119, 3584-3600, 2014.
1047 https://doi.org/10.1002/2013JB010901
1048

Schmid, T., Schreurs, G., Warsitzka, M., and Rosenau, M.: Effect of sieving height on density and friction of brittle analogue material: ring-shear test data of quarz sand used for analogue experiments in the Tectonic Modelling Lab of the University of Bern, 2020a.
https://doi.org/10.5880/fidgeo.2020.006

Schmid, T., Schreurs, G., Warsitzka, M., and Rosenau, M.: Effect of sieving height on density and friction of brittle analogue material: Ring-shear test data of corundum sand used for analogue experiments in the Tectonic Modelling Lab of the University of Bern (CH), 2020b.
https://doi.org/10.5880/fidgeo.2020.005

Schultz-Ela, D. and Walsh, P.: Modeling of grabens extending above evaporites in Canyonlands National Park, Utah, Journal of Structural Geology, 24, 247-275, 2002.
https://doi.org/10.1016/S0191-8141(01)00066-9

Tingay, M., Muller, B., Reinecker, J., and Heidbach, O.: State and origin of the present-day stress field in sedimentary basins: New results from the World Stress Map Project, Golden Rocks 2006, The 41st US Symposium on Rock Mechanics (USRMS).

Tingay, M. R., Morley, C. K., Hillis, R. R., and Meyer, J.: Present-day stress orientation in Thailand's basins, Journal of Structural Geology, 32, 235-248, 2010.
https://doi.org/10.1016/j.jsg.2009.11.008

Tron, V. and Brun, J.-P.: Experiments on oblique rifting in brittle-ductile systems, Tectonophysics, 188, 71-84, 1991.
https://doi.org/10.1016/0040-1951(91)90315-J

Trudgill, B. D.: Structural controls on drainage development in the Canyonlands grabens of southeast Utah, AAPG bulletin, 86, 1095-1112, 2002.
https://doi.org/10.1306/61EEDC2E-173E-11D7-8645000102C1865D

Willemse, E. J.: Segmented normal faults: Correspondence between three-dimensional mechanical models and field data, Journal of Geophysical Research: Solid Earth, 102, 675-692, 1997.
https://doi.org/10.1029/96JB01651

Willemse, E. J., Pollard, D. D., and Aydin, A.: Three-dimensional analyses of slip distributions on normal fault arrays with consequences for fault scaling, Journal of Structural Geology, 18, 295-309, 1996.
https://doi.org/10.1016/S0191-8141(96)80051-4

Withjack, M. O. and Jamison, W. R.: Deformation produced by oblique rifting, Tectonophysics, 126, 99-124, 1986.
https://doi.org/10.1016/0040-1951(86)90222-2

Zoback, M. L.: First-and second-order patterns of stress in the lithosphere: The World Stress Map Project, Journal of Geophysical Research: Solid Earth, 97, 11703-11728, 1992.
https://doi.org/10.1029/92JB00132

Zwaan, F. and Schreurs, G.: How oblique extension and structural inheritance influence rift segment interaction: Insights from 4D analog models, Interpretation, 5, SD119-SD138, 2017.
https://doi.org/10.1190/INT-2016-0063.1

Zwaan, F., Schreurs, G., Naliboff, J., and Buiter, S. J. H.: Insights into the effects of oblique extension on continental rift interaction from 3D analogue and numerical models, Tectonophysics, 693, 239-260, 10.1016/j.tecto.2016.02.036, 2016.
https://doi.org/10.1016/j.tecto.2016.02.036

Zwaan, F., Schreurs, G., Ritter, M., Santimano, T., and Rosenau, M.: Rheology of PDMS-corundum sand mixtures from the Tectonic Modelling Lab of the University of Bern (CH), 2018.
http://doi.org/10.5880/fidgeo.2018.023